JGR Solid Earth

RESEARCH ARTICLE
10.1029/2025JB032225

Tomographic Constraints on a Mid-Crustal High-Velocity Body Beneath West-Central Taiwan: Implications for Passive-Margin Mafic Additions

E.-J. Lee[1], W.-Y. Liao[1], I. Koulakov[2,3], P. Chen[4], S.-P. Chang[1], D.-Y. Chen[5], Y.-M. Wu[6,7], W.-T. Liang[7], Y.-T. Lo[8], H.-Y. Yen[8], and Y.-H. Lee[9]

[1]Department of Earth Sciences, National Cheng Kung University, Tainan, Taiwan, [2]Skolkovo Institute of Science and Technology (Skoltech), Moscow, Russia, [3]Trofimuk Institute of Petroleum Geology and Geophysics SB RAS, Novosibirsk, Russia, [4]Department of Geology and Geophysics, University of Wyoming, Laramie, WY, USA, [5]Central Weather Administration, Taipei, Taiwan, [6]Department of Geosciences, National Taiwan University, Taipei, Taiwan, [7]Institute of Earth Sciences, Academia Sinica, Taipei, Taiwan, [8]Department of Earth Sciences, National Central University, Taoyuan City, Taiwan, [9]Department of Earth and Environmental Sciences, National Chung Cheng University, Chiayi, Taiwan

Key Points:

- 3-D seismic tomography images a mid-crustal (~20–30 km) high-velocity, relatively dense body beneath west-central Taiwan
- Vp–Vs–ρ comparisons are consistent with mafic compositions; compatible with passive-margin mafic additions (underplating/intrusions)
- Structures inferred from tomographic profiles largely coincide with mapped faults and geological unit boundaries in Taiwan

Supporting Information:

Supporting Information may be found in the online version of this article.

Correspondence to:

E.-J. Lee,
rickli92@gmail.com

Citation:

Lee, E.-J., Liao, W.-Y., Koulakov, I., Chen, P., Chang, S.-P., Chen, D.-Y., et al. (2025). Tomographic constraints on a mid-crustal high-velocity body beneath west-central Taiwan: Implications for passive-margin mafic additions. *Journal of Geophysical Research: Solid Earth*, *130*, e2025JB032225. https://doi.org/10.1029/2025JB032225

Received 16 JUN 2025
Accepted 9 DEC 2025

Author Contributions:

Conceptualization: E.-J. Lee, S.-P. Chang, Y.-T. Lo, H.-Y. Yen, Y.-H. Lee
Data curation: D.-Y. Chen, Y.-M. Wu, W.-T. Liang
Formal analysis: Y.-T. Lo
Investigation: E.-J. Lee
Methodology: W.-Y. Liao, I. Koulakov
Resources: E.-J. Lee, P. Chen
Software: W.-Y. Liao, I. Koulakov, P. Chen
Validation: E.-J. Lee, P. Chen, Y.-T. Lo, H.-Y. Yen
Visualization: E.-J. Lee, I. Koulakov
Writing – original draft: E.-J. Lee

Abstract Using dense seismic data sets, we present a new 3D velocity model of Taiwan that images a prominent mid-crustal (~20–30 km) high-velocity body beneath west-central Taiwan. The inclusion of high-quality post-2012 recordings from the Central Weather Administration Seismic Network (CWASN) ensures the elimination of uncorrectable timing errors. In addition, a machine learning–based phase picker was applied to the entire data set to improve the consistency and accuracy of phase arrival identification. The resulting model generally aligns with previous tomographic studies. Structures inferred from velocity gradients in the tomographic profiles largely correspond to mapped faults and geological unit boundaries in Taiwan. The model also images a pronounced mid-crustal (~20–30 km) high-velocity anomaly beneath west-central Taiwan. Under representative P–T conditions, Vp–Vs–density comparisons indicate the best match with mafic compositions, though the interpretation is not unique. This mafic interpretation is compatible with passive-margin mafic additions (underplating and/or intrusions). The anomaly coincides with reduced seismicity below ~20 km and depth-dependent stress orientations, consistent with a relatively competent mid-crustal volume. Geological and geophysical similarities with the Dongsha Rise further suggest a possible shared tectonic and magmatic origin, likely linked to mafic underplating during South China Sea rifting. These findings improve our understanding of structural highs along passive continental margins and their role in influencing crustal deformation in the Taiwan orogen. The new model also provides a robust framework for future waveform-based seismic imaging.

Plain Language Summary This study uses a large amount of seismic data to create a new 3D model of Taiwan, imaging a high seismic velocity body at 20–30 km depth beneath west-central Taiwan. The model incorporates high-quality seismic data, which reduce timing uncertainties, and employs a machine learning–based algorithm to improve the accuracy and consistency of P- and S-wave arrival picks. Our seismic tomography generally agrees with previous studies, and structures inferred from wave-speed gradients align with mapped faults and geological boundaries. The model also images a high-velocity zone in the middle crust beneath west-central Taiwan. Comparisons of observed wave speeds and densities with modeled rock properties suggest the best match is mafic compositions, though other lithologies cannot be excluded. This feature may reflect magmatic additions during earlier passive-margin times, either as underplated layers or intrusions. Geophysical and geological similarities with the Dongsha Rise, another structural high along the passive margin, suggest that this feature may have formed during early margin evolution through magmatic underplating. These findings provide new insight into inherited structures within passive continental margins and their role in influencing crustal deformation and strain localization within the Taiwan orogen.

1. Introduction

Arc-continent collisions are fundamental geological processes that lead to crustal shortening, thickening, and complex deformation. These settings provide valuable opportunities to investigate mountain-building mechanisms, the evolution of fault systems, and lithospheric dynamics (e.g., Brown & Ryan, 2011). Among global examples, the Taiwan orogen is one of the most active and well-studied arc-continent collision zones, resulting from the ongoing convergence between the Philippine Sea Plate and the Eurasian continental margin (Figure 1)

Writing – review & editing: E.-J. Lee, I. Koulakov, S.-P. Chang, Y.-T. Lo

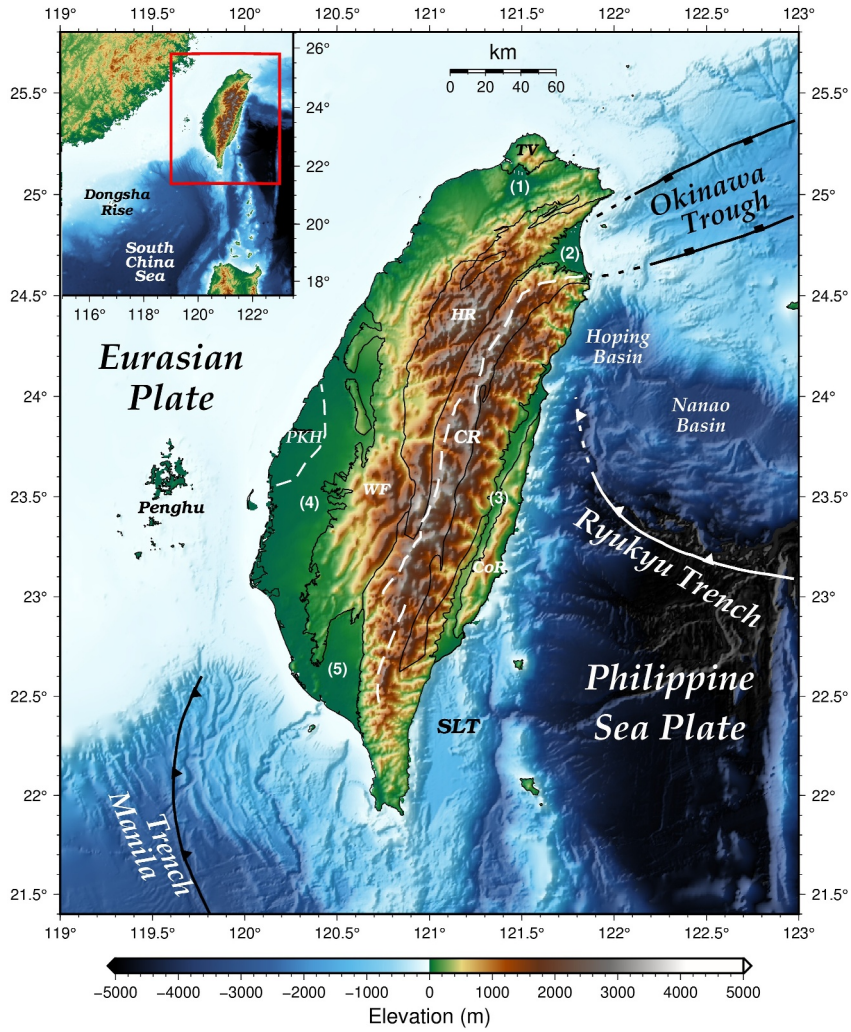

Figure 1. Tectonic setting and topography of Taiwan and its surrounding region. The inset map in the upper-left corner shows the regional topography, with the red box indicating the focus area of this study. The main map displays the topographic and geological framework of Taiwan. Major basins are labeled: (1) Taipei Basin, (2) Lanyang Plain, (3) Longitudinal Valley, (4) Coastal Plain, and (5) Pingtung Plain. Abbreviations: WF—Western Foothills; HR—Hsueshan Range; CR—Central Range; CoR—Coastal Range; PKH—Peikang High; TV—Tatun Volcano; SLT—Southern Longitudinal Trough. The white dashed line within the Central Range marks the trace of the Tayulin Fault (TF), as identified by Lee et al. (2022).

(e.g., Byrne et al., 2011; Eakin et al., 2014; Ho, 1986; Huang et al., 1997; Lee et al., 2022; Malavieille et al., 2002; Teng, 1990).

Early interpretations of the Taiwan orogeny emphasized a thin-skinned tectonic model, wherein an imbricate thrust-and-fold belt developed above a shallow east-dipping detachment fault (e.g., Barr & Dahlen, 1990; Carena et al., 2002; Suppe, 1980, 1981). This model was supported by surface geology and seismic profiles from the Western Foothills, effectively explaining the frontal fold-and-thrust belts (e.g., Suppe, 1980, 1981). However, subsequent geophysical evidence, including seismicity, gravity anomalies, and tomography, has revealed that deformation in Taiwan extends into the middle and lower crust (e.g., Lallemand et al., 2001; Rau & Wu, 1995; Wu et al., 1997; Yen et al., 1998), challenging the traditional shallow-crust interpretation.

Seismic tomography models have imaged a thickened crust beneath Taiwan, extending to depths of 50–60 km and indicating the presence of a crustal root. However, the limited resolution of earlier models has often hindered efforts to directly correlate subsurface velocity anomalies with mapped surface geology. When tomographic resolution is sufficiently high, such models can significantly improve geological interpretations by capturing detailed crustal architecture. For example, a high-resolution tomographic profile by Van Avendonk et al. (2016),

further analyzed by Lee et al. (2022), demonstrated that velocity anomalies in northern Taiwan are spatially consistent with surface structures, such as the anticlines in the Hsueshan Range and the Tayulin out-of-sequence thrust in the Central Range (Figure 1). This case highlights the potential of high-resolution seismic tomography to establish meaningful connections between subsurface structures and surface geology (Lee et al., 2022; Tan et al., 2024).

Recent research has underscored the critical role of tectonic inheritance from the passive continental margin in shaping the orogenic deformation observed in Taiwan. Pre-existing basement structures, such as variations in basement geometry and inherited extensional faults, have been shown to significantly influence the evolution of foreland basins, fold-and-thrust systems, and the spatial distribution of seismicity (e.g., Alvarez-Marron et al., 2014; Brown et al., 2012, 2017, 2022; Lin et al., 2003; Lin & Watts, 2002; Yang et al., 2006, 2016). High-resolution seismic tomography plays a crucial role in resolving these crustal features, offering new insights into the structural framework of the Taiwan orogen.

2. Background

The primary deformation structures in the Taiwan orogen are interpreted to have developed above a regional basal detachment fault. A series of ramp–flat geometries evolved above this detachment surface, producing west-verging fold-and-thrust systems that shape the topography of the orogenic belt (e.g., Brown et al., 2012; Lee et al., 2022; Tan et al., 2024). The Coastal Range to the east acts as a mechanically rigid backstop, focusing compressional stress westward into the orogenic wedge. From west to east, Taiwan consists of distinct geological provinces: the Coastal Plain, Western Foothills, Hsueshan Range, Central Range, and Coastal Range, which reflect progressive crustal shortening and uplift (Figure 1) (e.g., Ho, 1986; Huang et al., 1997; Lee et al., 2022; Tan et al., 2024; Teng, 1990). In addition to dominant forward-propagating thrusts, recent studies identified an out-of-sequence thrust system, the Tayulin Fault (TF), located in the Central Range (Figure 1). This fault was reactivated in the later stages of orogenesis and is associated with rapid uplift and exhumation (Lee et al., 2022; Tan et al., 2024).

Furthermore, within the framework of arc-continent collision, the structural inheritance from passive margin features, particularly basement geometry and pre-existing structural fabrics, shapes Taiwan's complex orogenic structure. As an extension of the northern South China Sea margin (Figure 1), the crustal architecture of this passive continental margin fundamentally governs the evolution of the Taiwan mountain belt and its foreland basins (e.g., Brown et al., 2017, 2022; Byrne et al., 2011; Lin et al., 2003; Lin & Watts, 2002; Mouthereau & Petit, 2003; Yang et al., 2006, 2016). The Peikang Basement High significantly influences sediment distribution and serves as a mechanical barrier, affecting deformation front propagation and the fold-and-thrust belt (Figure 1) (e.g., Alvarez-Marron et al., 2014; Biete et al., 2018; Brown et al., 2012, 2017, 2022; Camanni et al., 2016; Lacombe et al., 2003; Mirakian et al., 2013; Yang et al., 2016). Integrated studies utilizing 3D seismic tomography and seismicity patterns have mapped the basement-sediment interface with seismic velocities ($Vp > 5.2$ km/s), demonstrating how basement morphology directly controls basal thrust geometry in the Taiwan orogen (e.g., Alvarez-Marron et al., 2014; Biete et al., 2018, 2019; Camanni et al., 2016). Additionally, early extensional tectonics related to the opening of the South China Sea created suites of normal faults that were subsequently reactivated under compressional stress conditions, influencing the fault geometries and the spatial distribution of seismicity. The Peikang Basement High is part of the full thickness of the margin, located between the Eocene-aged Taishi Basin and the Miocene-aged Tainan Basin, along the necking zone of the margin (e.g., Alvarez-Marron et al., 2014; Brown et al., 2017, 2022; Lacombe & Bellahsen, 2016; Lee et al., 2025; Liao et al., 2025; Mouthereau et al., 2002; Mouthereau & Lacombe, 2006; Yang et al., 2016).

While previous studies extensively addressed upper crustal structures and sedimentary layers (e.g., Alvarez-Marron et al., 2014; Brown et al., 2012, 2017, 2022; Lacombe et al., 2003; Lin et al., 2003; Lin & Watts, 2002; Mirakian et al., 2013; Mouthereau et al., 2002; Yang et al., 2006, 2016), deeper crustal structures resulting from early extensional processes remain comparatively understudied. Gravity anomaly analyses in west-central Taiwan indicate the presence of high-density materials in deeper crustal layers (Hsieh & Yen, 2016). Combined seismic tomography and gravity data further support the presence of high-velocity zones in the middle crust (Cheng, 2004; Cheng et al., 2003). In addition, a high-amplitude magnetic anomaly has been reported in west-central Taiwan, coincident with the Peikang Basement High and extending eastward (e.g., Hsu et al., 1998). After reduction-to-the-pole correction, the anomaly shifts northward relative to the uncorrected field (e.g., Doo

et al., 2025; Hsu et al., 2008). Recent analyses further indicate a mid-crustal source at ∼20–30 km depth (Doo et al., 2025).

In this study, we present a new seismic tomography model of Taiwan, made possible by increased seismic station density and improved data quality, enabling a more refined understanding of deep crustal structures. Although numerous tomographic studies have previously been conducted (e.g., Huang et al., 2014; Kim et al., 2005; Koulakov et al., 2014, 2015; Kuo-Chen et al., 2012; Rau & Wu, 1995; Roecker et al., 1987; Wu et al., 2007, 2009), further updates remain essential. Most prior tomographic models have relied on P- and S-wave arrival times from the Central Weather Administration (CWA) catalog, which were manually picked by multiple analysts. The large data set size and variability in individual picking criteria, particularly for S-wave arrivals that are often affected by coda waves and scattering, have introduced inconsistencies that may compromise model resolution and reliability. To address this limitation, we employ a machine learning–based phase-picking algorithm, specifically trained and validated on seismic data from Taiwan, which substantially improves the accuracy and consistency of both P- and S-wave picks (Liao et al., 2021, 2022). In addition, seismic data quality has markedly improved since 2012, following the upgrade of Taiwan's Central Weather Administration Seismic Network (CWASN) to 24-bit recording systems with GPS-synchronized timing (Chang et al., 2012). Extensive synthetic testing, including inversions using independent data subsets (e.g., odd/even event tests), confirms the robustness and reliability of the derived structures. Our inversion was performed using the LOTOS code, which employs quasi-continuous rotated grids to produce stable, grid-independent velocity models (Koulakov, 2009). Comparisons with previous models further validate the consistency and reliability of our results. Overall, this updated seismic tomography, supported by advanced data sets, rigorous processing techniques, and comprehensive validation, provides new insights into the crustal architecture and geodynamic processes of the Taiwan orogenic belt.

3. Data, Methods, and Resolution Analysis

3.1. Integrated Seismic Networks

The resolution of seismic tomography strongly depends on data coverage. Therefore, seismic recordings from both permanent and temporary seismic networks have been utilized for this study. The networks used include: (a) CWASN (Central Weather Administration Seismic Network) (Shin et al., 2013), (b) TSMIP (Taiwan Strong Motion Instrumentation Program) (Liu et al., 1999), (c) BATS (Broadband Array in Taiwan for Seismology) (Kao et al., 1998), (d) TAIGER (TAiwan Integrated GEodynamics Research) (Okaya et al., 2006), (e) P-alert (Wu et al., 2013), and (f) Japan Meteorological Agency Seismic Network (JP network). Figure 2 illustrates the distribution of stations from these networks used in this study.

CWASN, established in 1991 for routine earthquake detection and monitoring (Shin et al., 2013), initially transmitted seismic data via telephone lines with timestamps assigned at the Taipei data center. Prior to 2012, this setup introduced random telemetry delays (0.06–0.24 s) that varied over time and across stations (Chang et al., 2012). In 2012, CWASN was upgraded to 24-bit recording and on-site GPS timing (Chang et al., 2012). While CWASN phase picks are widely used in tomographic studies (e.g., Huang et al., 2014; Kim et al., 2005; Koulakov et al., 2015; Kuo-Chen et al., 2012; Rau & Wu, 1995; Roecker et al., 1987; Wu et al., 2007, 2009), incorporating pre-2012 data with random delays may bias inversions, especially when combined with other networks like BATS. To avoid these errors, this study uses only CWASN data recorded after 2012.

We incorporate earthquake recordings from the TAIGER project (2006–2009), which include broadband, short-period, and ocean-bottom seismometers (Okaya et al., 2006). Additional data come from Taiwan's TSMIP and P-alert accelerometer networks, which provide dense coverage in metropolitan areas (Figure 2). TSMIP, established in 1991 for seismic hazard assessment (Liu et al., 1999), operated mostly in triggered mode before 2018, leading to timing uncertainties. Since then, it has transitioned toward real-time recording. P-alert, launched around 2010, offers real-time data for early warning and rapid damage assessment (Wu et al., 2013). We also include data from Japan's southernmost JMA station to improve coverage near the Ryukyu Trench and Okinawa Trough.

By integrating data from multiple seismic networks, our study aims to achieve comprehensive coverage and enhanced resolution for crustal scale seismic tomography in Taiwan. The diverse data sources, along with the

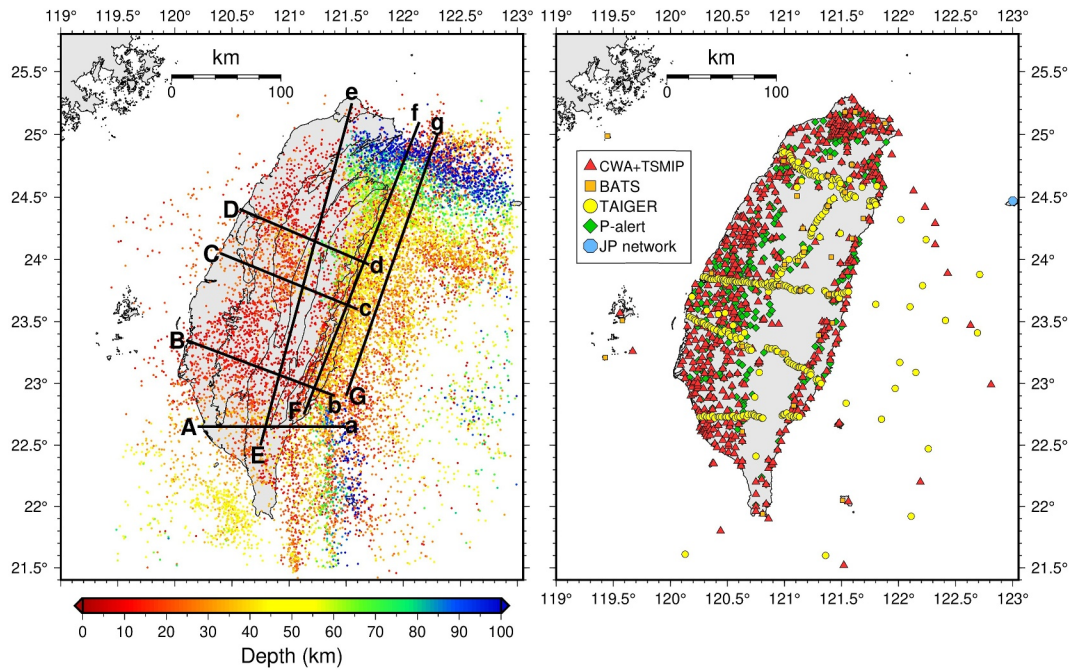

Figure 2. Distribution of earthquake events (left) and seismic stations from various networks (right) used in this study for seismic tomographic inversion. The thick black lines on the left map indicate the locations of the profiles shown in Figure 7.

inclusion of post-2012 CWASN recordings to avoid telemetry delay issues, will contribute to a more reliable crustal-scale tomography of Taiwan.

3.2. Earthquake Selection Process

Seismic tomography relies on crossing ray paths to resolve seismic velocity. We applied the following event selection procedures to ensure efficient ray path coverage for our tomographic inversion in the high seismicity region of Taiwan:

1. Spatial Division: The study area was divided into 0.05° × 0.05° × 5 km cubes.
2. Initial Event Selection: For each cube, the five events with the largest number of P and S picks in the CWA catalog were selected as candidate earthquakes.
3. Phase Picking: The RED-PAN phase picker, a deep learning-based seismic phase picking algorithm (Liao et al., 2021, 2022), was applied to available seismic recordings from different networks.
4. Final Event Selection: From the candidate events, the two with the largest number of qualified P and S picks in each cube were selected for our tomographic inversion.

Events with fewer than eight phase picks were rejected. This event selection procedure was applied to two time periods to select seismic recordings from various networks: March 2006 to September 2009: During the TAIGER project period, available seismic data from BATS, TAIGER, and JP network were selected. January 2012 to July 2022: Available seismic data from CWASN, BATS, TSMIP, P-alert, and JP network were selected. Figure 2 shows the distribution of earthquakes used in our tomographic inversion.

3.3. Seismic Phase Picking

Accurate P and S arrival picks are critical for reliable travel time tomography. Manual picking, though common, becomes impractical and prone to bias when handling large data sets. To address this, we use the RED-PAN machine learning model, trained on diverse seismic data from Taiwan, including broadband, short-period, and accelerometer recordings (Liao et al., 2021, 2022). RED-PAN achieves high precision on an independent Taiwan data set, with 98% accuracy for P-wave and 95% for S-wave picks using thresholds of <0.1 s error and phase probability >0.5 (Liao et al., 2022). Compared to manual picks, machine learning based picks offer greater consistency (Liao et al., 2021) and reduced error, improving inversion quality.

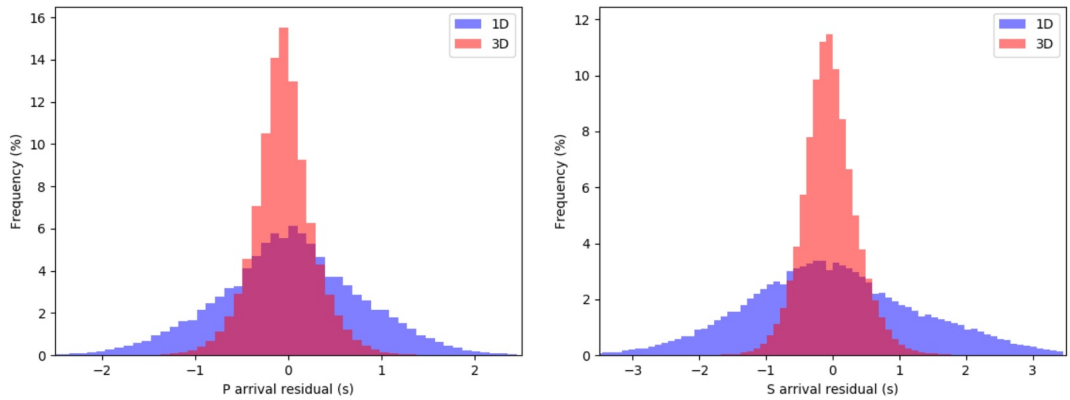

Figure 3. P-wave (left) and S-wave (right) arrival time residuals for the initial 1D layered model (blue histograms) and the final 3D velocity model (red histograms) obtained in this study.

We use the following procedures and thresholds to select reliable P and S picks for our tomographic inversion:

1. Initial Selection: P and S arrivals with probabilities predicted by RED-PAN greater than 0.5 are selected as potential picks for an earthquake.
2. Signal-to-Noise Ratio (SNR): The signal-to-noise ratios (SNRs) of selected P and S waves are used for phase selection. A bandpass corner frequency filter is applied to the waveforms. The SNR is based on the root mean square (RMS) of three-component seismograms. The noise is a 10-s waveform ending 1.0 s before the predicted P arrival, the signal for the P phase is a 3-s waveform starting 0.5 s before the predicted P arrival, and the signal for the S phase is a 4-s waveform starting 0.5 s before the predicted S arrival. P arrivals with SNR less than 4 and S arrivals with SNR less than 6 are rejected.
3. Confirmation: Predicted P and S arrivals based on the initial layered model are used for confirmation. The thresholds for the differences between predicted and observed travel times are 2.5 s for P picks and 3.5 s for S picks.

A total of more than 12,000 seismic events were selected for analysis (Figure 2), yielding in excess of 643,000 P-wave and 479,000 S-wave arrival picks for the tomographic inversion. The distributions of P- and S-wave arrival time residuals for the selected picks are illustrated in Figure 3.

3.4. Tomographic Inversion

In this study, we applied the updated Local Tomography Software (LOTOS) developed by Koulakov (2009) for our Taiwan seismic tomographic inversion. Our tomographic model is centered at 120.0°E and 23.5°N, extending 250 km both east and west, and 300 km both south and north. The depth range is from 4 km above the surface to 140 km underground. The horizontal grid spacing is 5 km; in the vertical direction, the grid spacing varies depending on the ray density, but cannot be less than 4 km. The initial 1D layered model used in this study is the same as that in Huang et al. (2014), which is averaged from the 3D velocity model of Wu et al. (2009). The grids are parameterized with four azimuthal orientations (0°, 22°, 45°, and 67°) for tomographic inversions to avoid potential grid-dependent effects (Koulakov, 2009). In LOTOS, the bending method is used for ray tracing in 3D velocity models. In each iteration, before each seismic tomographic inversion, the hypocenters of the earthquakes used are relocated in the current 3D model. The first derivative matrix, A, is then calculated using the ray paths based on these hypocenters in the velocity models. Each element of the matrix, **A**ij, represents the time deviation along the *i*th ray due to a unit-velocity perturbation in the *j*th node. The inversion of the matrix is performed using the damped LSQR method (Nolet, 1985; Paige & Saunders, 1982) simultaneously for the P and S data and for the source parameters (dx, dy, dy and dt for each event). Note that in this study, the Vp/Vs ratio was calculated by simple division of the obtained absolute values of the Vp and Vs. A number of synthetic tests presented below demonstrate the adequacy of this method.

The damping and smoothing parameters for both P- and S-wave velocity models were determined through synthetic modeling, following the recommendations of Koulakov (2009). These synthetic tests were designed to mirror the real-data inversion process as closely as possible, using the same event and station distributions,

inversion procedures, and ray coverage. Importantly, in our testing workflow, source locations were treated as unknowns. As in the real inversion, we first performed absolute event relocation and then applied iterative inversion steps, which include source and velocity updates. This approach realistically captures the trade-off between source parameters and velocity structure, a critical aspect in passive-source tomography that is often overlooked in some previous studies. To identify the optimal inversion parameters, we conducted multiple synthetic checkerboard tests using different combinations of damping and smoothing values. The optimal results, achieving the most accurate recovery of the synthetic anomalies, were obtained using a damping factor of 1.5 and a smoothing coefficient of 5.0. These values were therefore adopted in the inversion of the real data set (Koulakov, 2009).

In our tomographic inversion, we performed three iterations to achieve optimal results. The number of iterations was determined based on the convergence of the time residuals for both P and S arrivals. The variance reduction in L1 norm of P-wave residuals after three iterations was from 0.465 to 0.213 s (52.98%), and that of the S-wave residuals was from 0.656 to 0.291 s (55.59%). These significant reductions in residuals demonstrate high quality of the data having high signal-to-noise ratio that was provided by the new automated picking procedure. For example, using a similar way of variance reduction calculation, in another tomography study of Taiwan by Koulakov et al. (2015) the reductions were from 0.622 to 0.414 s (33.44%) for the P-waves and from 1.043 to 0.663 s (36.43%) for the S-waves. In another study, Huang et al. (2014) reported a total 67% of variance reduction, however, it was calculated in the L2 norm giving larger values of reductions than the L1 norm used here.

3.5. Resolution Analysis

The resolution of tomographic models plays a critical role in interpreting subsurface structures. To evaluate the robustness and limitations of our inversion results, we conducted three types of synthetic resolution tests: a checkerboard test (Figure 4), a restoration test (Figure 5), and a spike test (Text S1 and Figure S1 in Supporting Information S1). The spike test demonstrates that finer-scale anomalies can be reliably resolved in regions with dense data coverage. All synthetic tests were designed using the same station and event distributions, and they follow identical inversion procedures as applied to the real data set.

We first conducted a 3D checkerboard test by assigning synthetic anomalies of ±10% in P- and S-wave velocities to alternating cubic cells, with a spacing of 25 km in both horizontal and vertical directions. The vertical checkerboard anomalies are initiated at 10 km above sea level to ensure that they span the entire elevation range of the model, The P- and S-wave anomalies were given opposite signs to introduce variation in the Vp/Vs ratio. Figure 4 presents the results of the checkerboard resolution tests, displaying recovered anomalies in map view at depths of 6, 25, and 50 km, as well as along vertical cross-sections traversing different parts of the model domain. Overall, the checkerboard patterns are reasonably well recovered to depths of approximately 50 km across most regions.

To further evaluate model robustness under more realistic geological scenarios, we constructed a 3D synthetic model consisting of free-form prisms that replicate the shapes of key structures identified in the real-data inversion. These synthetic anomalies span three depth intervals: the shallow crust (<16 km), mid-crust (16–45 km), and lower crust to upper mantle (45–80 km). Notably, the deepest layer extends beyond the vertical resolution limits inferred from the checkerboard test results in Figure 4. Despite their increased depth and geometric complexity, the synthetic anomalies are recovered across most of the study area and throughout all depth intervals (Figure 5). This indicates that even in deeper regions, where traditional checkerboard tests typically fail, meaningful structural resolution can still be achieved when anomalies are sufficiently large.

4. Tomographic Results and Model Validation

4.1. Tomographic Results

The resulting model is presented in terms of Vp, Vs, and the Vp/Vs ratio across four horizontal and seven vertical sections, as illustrated in Figures 6 and 7. To ensure comparability, the depths of the horizontal sections were defined in alignment with those used in Huang et al. (2014). For clarity, earthquakes are not displayed in the resulting panels to prevent overcrowding, except in specific vertical sections where they are included to support our interpretation.

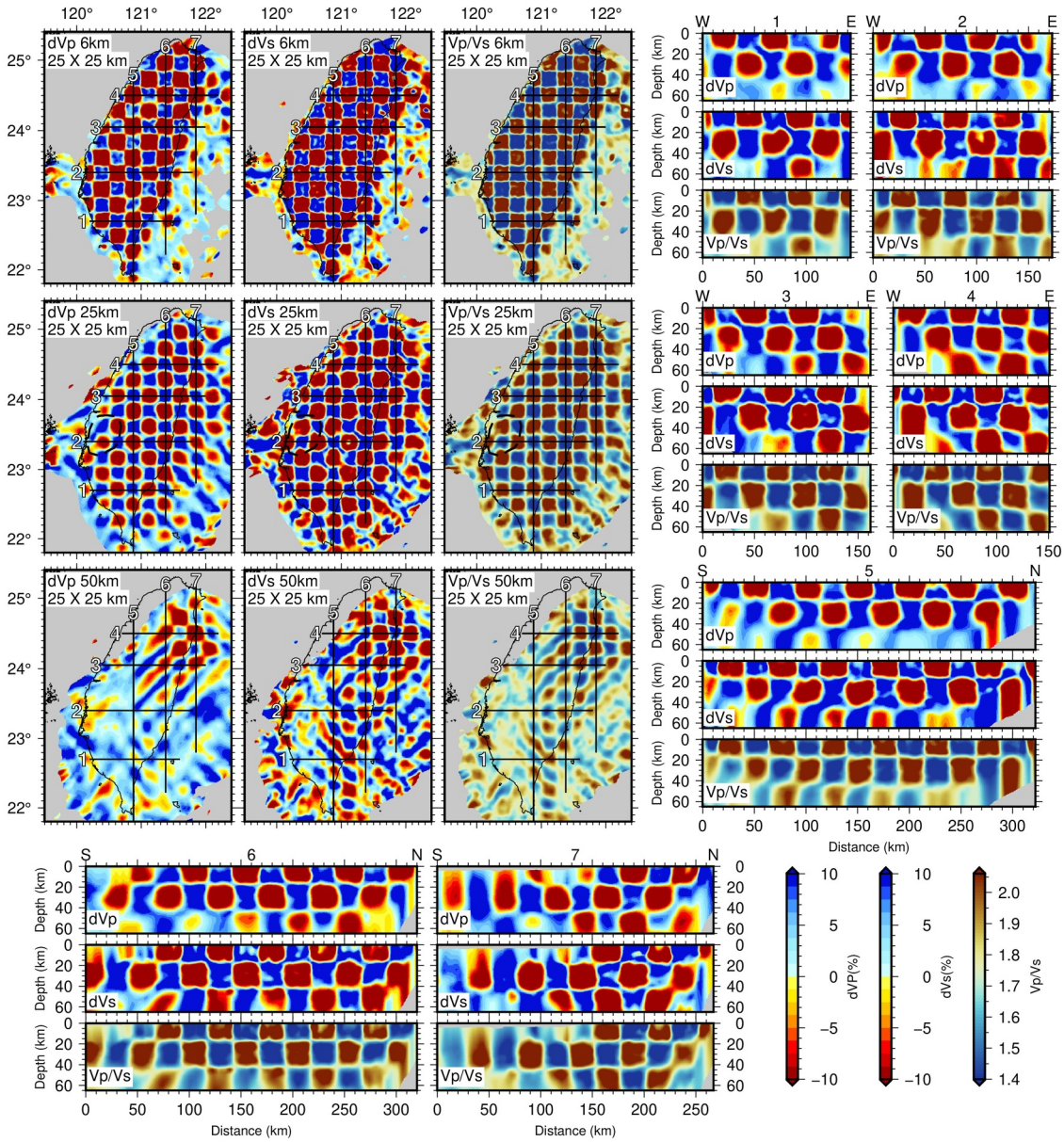

Figure 4. Vertical and Horizontal Checkerboard Resolution Test Results. This figure presents the results of checkerboard resolution tests for the dVp, dVs, and Vp/Vs models at various depths (6, 25, and 50 km), as well as along multiple vertical cross-sections. The horizontal test panels illustrate alternating high and low velocity anomalies across Taiwan, while the vertical cross-sections depict the model's resolution along selected transects (profiles 1–7) spanning different regions of the island. At a depth of 25 km, the dashed ellipse outlines the region corresponding to a high-velocity anomaly identified in the final 3D seismic velocity model beneath west-central Taiwan.

At 0 km depth (Figure 6), the velocity model images Taiwan's major basins and plains as contiguous low-velocity zones. The Taipei Basin, Lanyang Plain, Coastal Plain, and Pingtung Plain exhibit Vp < 3.8 km/s and Vs < 2.2 km/s, accompanied by elevated Vp/Vs ratios (>1.73). The Western Foothills show similar shallow low-velocity characteristics. In contrast, the Hsueshan Range and Central Range appear as higher-velocity domains (Vp > 3.7 km/s, Vs > 2.3 km/s) with lower Vp/Vs ratios (<1.71). The Longitudinal Valley suture is expressed as a sharp lateral velocity contrast that coincides with the valley trace. The Coastal Range is characterized by relatively low Vp (<3.8 km/s) and Vs (<2.2 km/s), which could be attributed to its composition of accreted volcanic islands and forearc basin sediments (Figure 6, first row). These observations confirm that the inversion reliably reproduces the known near-surface geological provinces, supporting the robustness of the model in the shallow crust.

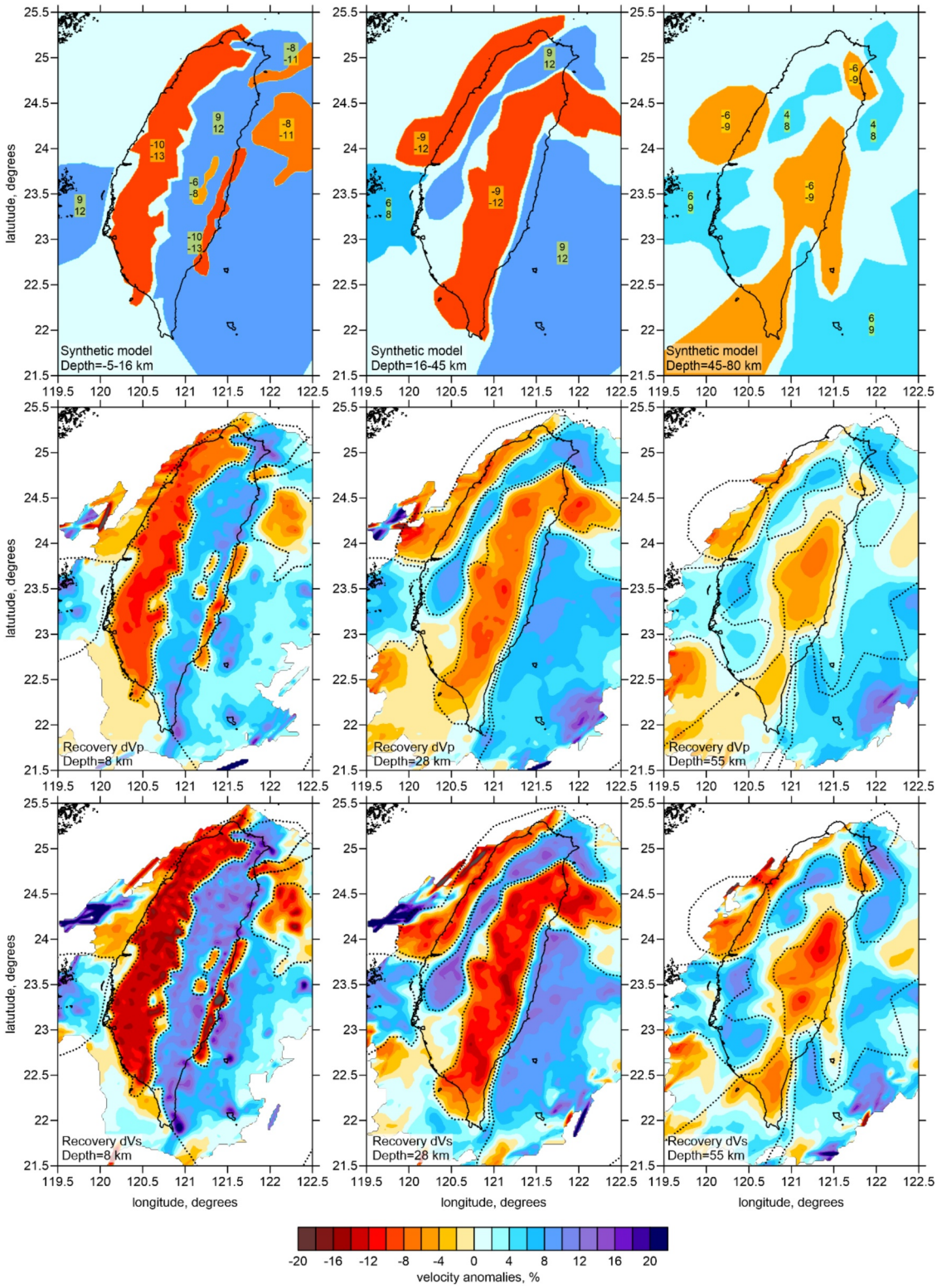

Figure 5. Synthetic test with free-shaped anomalies of realistic shapes. The upper row presents the synthetic model defined in selected depth intervals. The values of dVp and dVs in percent are indicated inside each pattern. The recovery of dVp and dVs at three depths are shown in the middle and lower rows. The shapes of the synthetic anomalies are indicated with the dotted lines.

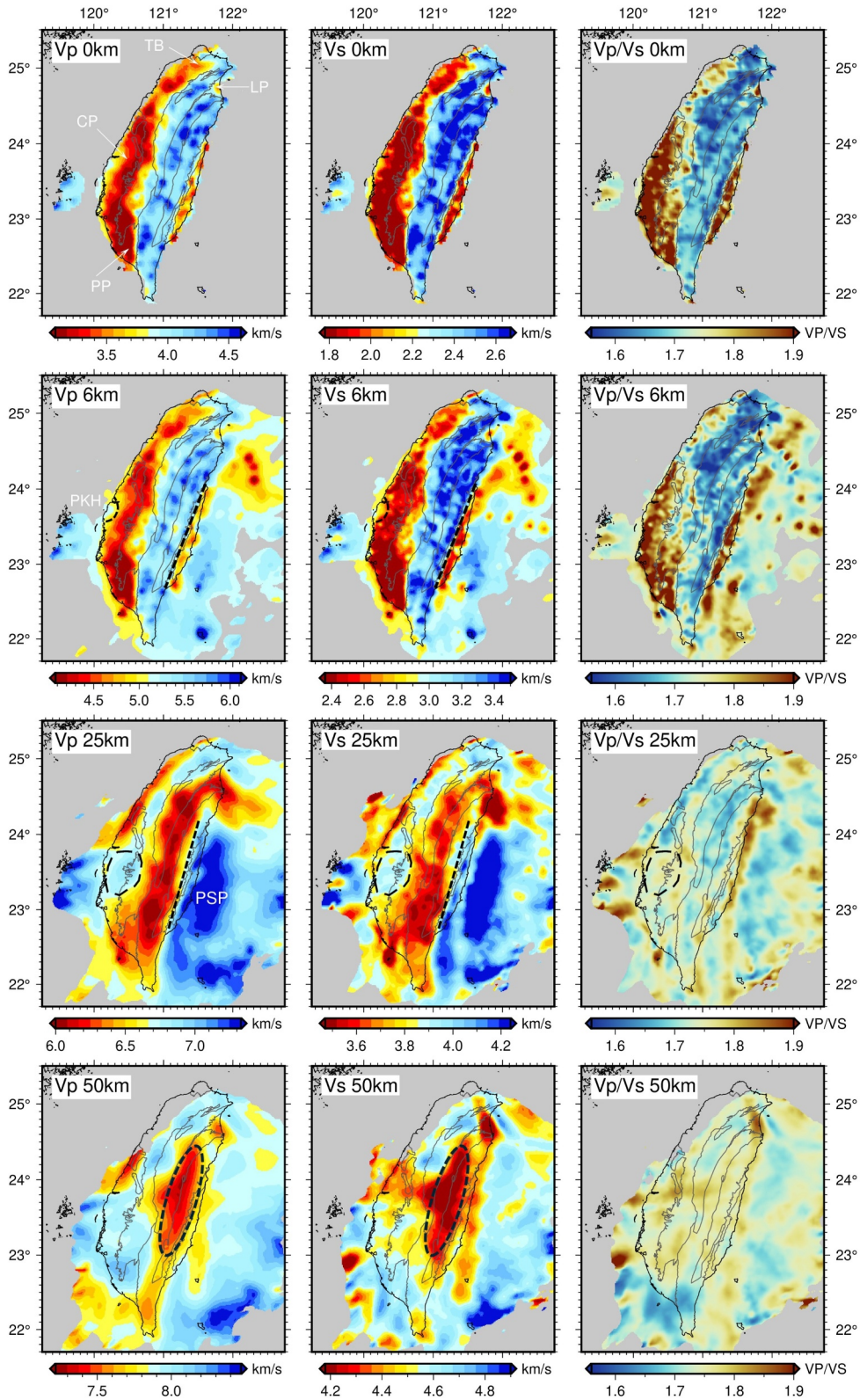

Figure 6. Map view of Vp, Vs, and Vp/Vs values from our 3D velocity model at different depths. Dashed lines highlight the structures discussed in the text. Abbreviations: TB–Taipei Basin, LP–Lanyang Plain, CP–Coastal Plain, PP–Pingtung Plain, PKH–Peikang High, and PSP–Philippine Sea Plate.

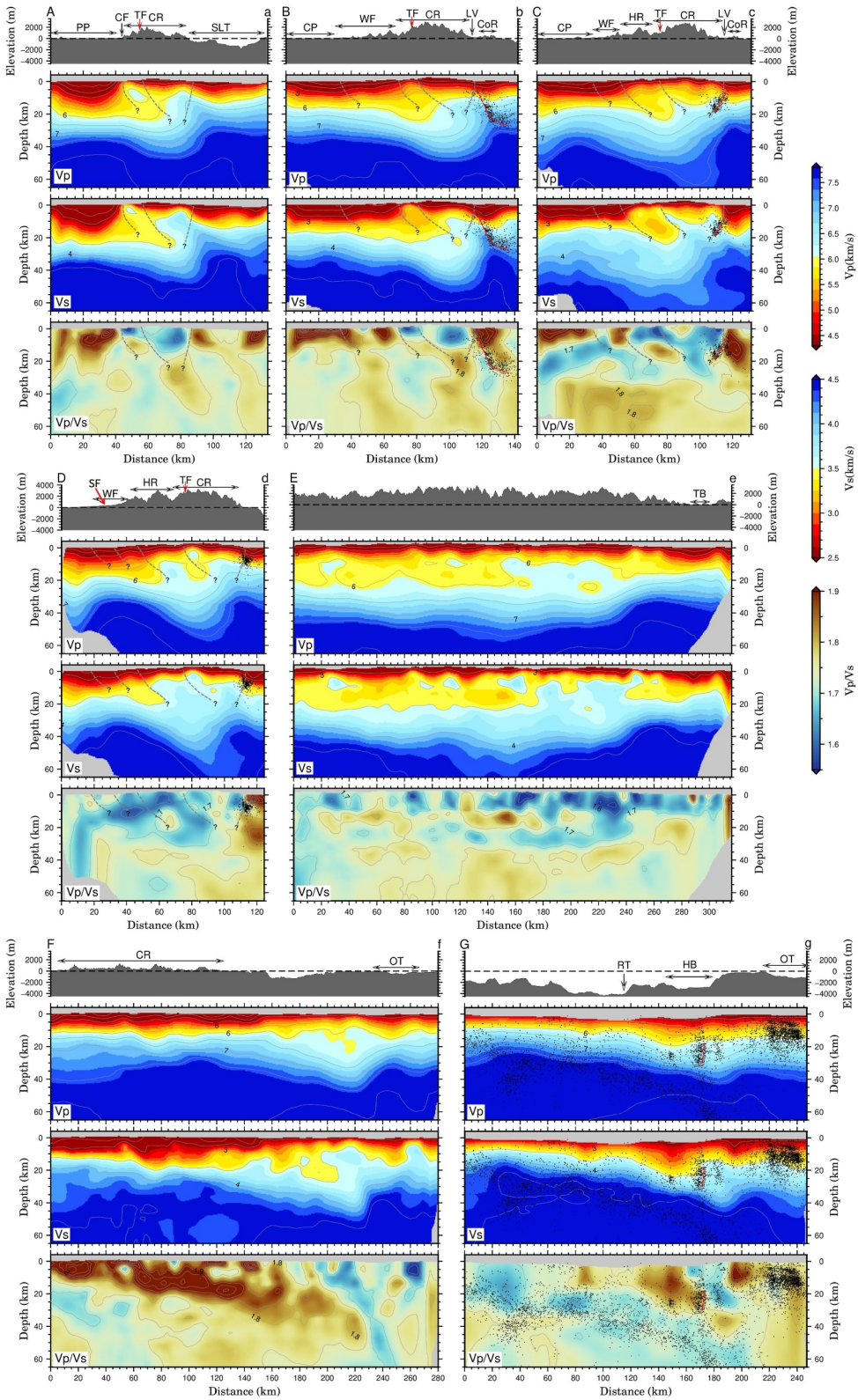
A
a
PP
CF
TF
CR
SLT
B
b
CP
WF
TF
CR
LV
CoR
C
c
CP
WF
HR
TF
CR
LV
CoR
D
d
SF
WF
HR
TF
CR
E
e
TB
F
f
CR
OT
G
g
RT
HB
OT
Elevation (m)
Depth (km)
Distance (km)
Vp
Vs
Vp/Vs
Vp(km/s)
Vs(km/s)
Vp/Vs

Figure 7.

Beyond near-surface structures, our seismic tomography results show good overall consistency with previous crustal-scale tomographic studies in Taiwan (e.g., Huang et al., 2014; Kim et al., 2005; Koulakov et al., 2015; Kuo-Chen et al., 2012; Rau & Wu, 1995; Roecker et al., 1987; Wu et al., 2007, 2009). The following features have been commonly imaged in earlier models and are also resolved in this study. At a depth of 6 km, our model reveals a zone of relatively high Vp (>5 km/s) beneath the Coastal Plain of west-central Taiwan (Figure 6, second row), corresponding to the Peikang Basement High (PKH), a prominent Mesozoic structural high (Lin et al., 2003; Lin & Watts, 2002; Yang et al., 2006). This feature has been consistently documented in prior tomographic studies (e.g., Huang et al., 2014; Kuo-Chen et al., 2012; Roecker et al., 1987; Wu et al., 2007, 2009). The Western Foothills and Coastal Plain are characterized by relatively low Vp (<4.8 km/s) and high Vp/Vs ratios (>1.8), reflecting the sedimentary composition of Taiwan's foreland basins (Figures 6 and 7, profiles Aa–Dd). Notably, the Pingtung Plain shows similar low Vp and high Vp/Vs anomalies extending to approximately 15 km depth (Profile Aa, Figure 7), which are suggestive of significant sedimentary accumulation. These features are consistent with previous velocity models (Huang et al., 2014; Wu et al., 2007).

At the crustal scale, our tomographic model generally agrees with the first-order architecture reported by previous 3D tomographic studies of Taiwan (e.g., Huang et al., 2014; Kim et al., 2005; Koulakov et al., 2015; Kuo-Chen et al., 2012; Rau & Wu, 1995; Wu et al., 2007, 2009). From south to north (profiles Aa–Dd, Figure 7), the model images an eastward-deepening Moho and associated crustal thickening beneath the orogen. The crustal thickness increases from ∼20 to 30 km beneath the western foreland to ∼40–50 km beneath the Central Range (e.g., Kuo-Chen et al., 2012; Rau & Wu, 1995). In addition, a sharp velocity gradient along the Longitudinal Valley suture zone (Figure 6, dashed lines at depths of 6 and 25 km) is imaged, consistent with earlier studies (e.g., Huang et al., 2014; Kuo-Chen et al., 2012).

Our seismic tomography also captures features associated with the subduction of the Philippine Sea Plate (PSP) beneath the Eurasian Plate (EP) along the Ryukyu Trench in northeastern Taiwan, in agreement with earlier studies (e.g., Huang et al., 2014; Kim et al., 2005; Koulakov et al., 2015; Kuo-Chen et al., 2012; Rau & Wu, 1995; Wu et al., 2007, 2009). Profile Ff (Figure 7) shows a high Vp/Vs ratio body (>1.75) beneath the Coastal Range, extending northward toward the Ryukyu Trench, likely representing volcanic arc and forearc basin materials. The northward-dipping trend of this high Vp/Vs body provides evidence for PSP subduction. Similarly, Profile Gg (Figure 7) exhibits northward-dipping structures, where low Vp/Vs ratios (<1.7) likely reflect the subducting oceanic crust of the PSP. The regional background seismicity also displays a consistent northward-dipping pattern. A noteworthy feature is a near-vertical cluster of earthquakes observed at depths between 15 and 30 km along the northern margin of the Hoping Basin (HB) (Figure 7, profile Gg). The spatial distribution of earthquakes (events with Grade A and B location errors) in the Geophysical Data Management System (GDMS) corresponds closely to a prominent discontinuity imaged in both Vs and Vp/Vs in our tomographic model. Notably, this feature has also been independently identified through a dense Ocean Bottom Seismometer (OBS) array deployed in the region (Lallemand et al., 2013; Profile 5), thereby providing external validation for the reliability of our model.

Beyond characterizing the general crustal structures of Taiwan, our 3D velocity model reveals features that correlate with several major earthquake sequences, demonstrating the model's potential in imaging seismogenic structures. The earthquake data utilized in this analysis were obtained from the GDMS maintained by the CWA (Shin et al., 2013). To ensure data reliability, only events with location quality ratings of A and B were included in the analysis (Central Weather Administration, 2012). Profile Bb in Figure 7 reveals a prominent eastward-dipping trend in the Longitudinal Valley region, particularly evident in the Vp/Vs distribution. This structural feature, previously documented in seismic tomography studies (e.g., Wu et al., 2007), shows remarkable correlation with the 2003 Mw 6.8 Chengkung earthquake sequence associated with the Longitudinal Valley Fault system. The spatial relationship between the velocity structure and seismicity patterns provides compelling evidence for the

Figure 7. Cross-sectional profiles of Vp, Vs, and Vp/Vs ratios, along with topography, extracted from the 3D seismic velocity model developed in this study. The locations of the profile lines are shown in Figure 2. Gray dashed lines indicate the structures inferred from the velocity model (see Text S4 in Supporting Information S1). Black dots represent earthquake hypocenters, while red dashed lines mark faults inferred from both seismicity patterns and velocity anomalies. Abbreviations: PP—Pingtung Plain; CF—Chaochou Fault; CR—Central Range; TF—Tayulin Fault; SF—Sanyi Fault; SLT—Southern Longitudinal Trough; CP—Coastal Plain; WF—Western Foothills; LV—Longitudinal Valley; CoR—Coastal Range; HR—Hsueshan Range; TB—Taipei Basin; OT—Okinawa Trough; RT—Ryukyu Trench; HB—Hoping Basin.

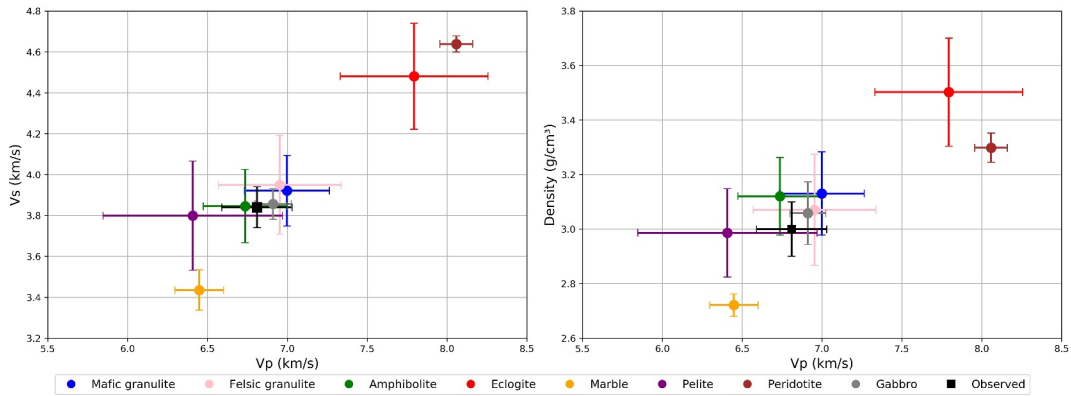

Figure 8. Vp–Vs and Vp–Density plots for the modeled lithologies under mid-crustal conditions. Colored symbols show lithologies from the Brown et al. (2024) rock database, with means ±1σ. The black square marks the average seismic velocity values (±1σ) for the west-central Taiwan target volume (20–30 km), and the density estimate is based on gravity analyses (Hsieh & Yen, 2016).

fault system's geometry and extent. Further north, Profile Cc (Figure 7) exhibits a high-angle westward-dipping velocity discontinuity in the Longitudinal Valley region. This structural feature demonstrates strong spatial correspondence with the 2013 Mw 6.2 Ruisui earthquake sequence. On profile Dd (Figure 7), the seismicity of the 2018 Mw 6.4 Hualien earthquake sequence also spatially coincides with Vp/Vs gradients in our model.

4.2. High-Velocity Structure in the Middle Crust of West-Central Taiwan

The geometry and shallow extent of the Peikang Basement High have been well constrained by previous seismic and drilling investigations (e.g., Lacombe et al., 2003; Lin et al., 2003; Lin & Watts, 2002; Yang et al., 2006, 2016). Upper crustal high-velocity anomalies associated with this feature have been consistently imaged in past tomographic models (e.g., Huang et al., 2014; Kuo-Chen et al., 2012; Roecker et al., 1987; Wu et al., 2007). However, the deeper crustal structure beneath west-central Taiwan has remained poorly resolved. Our tomography reveals a mid-crustal (~20–30 km) high-velocity body beneath west-central Taiwan (Figure 6, third row). Although similar anomalies are present in previous models (e.g., Huang et al., 2014; Kuo-Chen et al., 2012), notable discrepancies in their extent and velocities are observed relative to our results (Text S2 and Figure S2 in Supporting Information S1). This anomaly is spatially correlated with the surface projection of the Peikang Basement High, but it extends farther eastward and occupies a broader region at depth. This spatial correspondence highlights a possible link between the mid-crustal anomaly and the Peikang Basement High, implying that they may be associated with related tectonic processes, as further discussed in Section 5.3.

To assess possible rock types for the high-velocity body in the middle crust of west-central Taiwan, we used the rock database compiled by Brown et al. (2024) to model seismic velocities and densities at given pressures and temperatures. The data set includes common middle–lower crustal lithologies as well as potential rock types relevant to the Taiwan region, compiled from diverse locations. This approach minimizes geographic bias and provides representative compositions for comparative analyses. The average Vp and Vs within the targeted zone, corresponding to the circled area in the third row of Figure 6 and spanning depths from 20 to 30 km, were calculated using a horizontal grid spacing of 0.1° and a vertical resolution of 1 km. The resulting averages are Vp = 6.81 ± 0.22 km/s and Vs = 3.84 ± 0.10 km/s. Gravity data indicate a corresponding density range of approximately 2.9–3.1 g/cm^3 (Hsieh & Yen, 2016). Assuming a geothermal gradient of 25°C/km and a crustal density of 2.8 g/cm^3, the estimated temperature and pressure at 25 km depth are ~650°C and ~0.686 GPa, respectively. We applied the worksheet and macros developed by Abers and Hacker (2016) to estimate Vp, Vs, and density under pressure–temperature conditions relevant to the middle crust. Figure 8 presents Vp–Vs and Vp–density cross-plots for representative lithologies, overlaid with our seismic velocity and density estimates. Our estimates fall within the fields of mafic granulite (Vp = 7.00 ± 0.27 km/s; Vs = 3.92 ± 0.17 km/s; ρ = 3.13 ± 0.15 g/cm^3), amphibolite (6.74 ± 0.26; 3.85 ± 0.18; 3.12 ± 0.14), and gabbro (6.91 ± 0.11; 3.86 ± 0.08; 3.06 ± 0.12), which provide the closest joint matches in both panels. Felsic granulite (6.95 ± 0.38; 3.95 ± 0.24; 3.07 ± 0.20) also overlaps our estimates within uncertainties, but the match is sensitive to garnet

modal abundance. Garnet enrichment raises both Vp and density, shifting felsic compositions into the acceptance region, whereas garnet-poor felsic rocks tend to underpredict them (e.g., Brown et al., 2024). By contrast, eclogite and peridotite are systematically too fast and dense, whereas marble is too slow and light. Pelite overlaps only marginally owing to its lower Vp. These mid-crustal averages fall within the fields of amphibolite, mafic granulite, gabbro in Vp–Vs–ρ space, but the match is non-unique; we therefore defer lithologic and origin interpretations to Section 5.

4.3. Model Validations

Model validation is a critical component of seismic tomography, as it provides independent evidence for the reliability and robustness of the derived velocity structures. In this study, we applied three complementary approaches to evaluate the credibility of our tomographic results. First, we performed an internal consistency test by dividing the data set into odd- and even-event subsets. Independent inversions were conducted using each subset to assess the stability of the recovered structures. This approach helps ensure that the resulting model is not overly dependent on specific data subsets, and that the major structural features are consistently recovered regardless of data partitioning (Text S3 and Figure S3 in Supporting Information S1). Second, we converted our P-wave velocity (Vp) model into an equivalent density distribution using an empirical Vp–density relationship. The resulting density model was then compared with observed Bouguer gravity anomalies. Lastly, we compared our tomographic model with ambient noise Green's functions, which were derived independently and do not involve any of the travel-time data used in the inversion. These validation strategies provide independent support for the reliability of our seismic velocity model.

4.3.1. Model Comparison With Gravity Observations

The comparison of computed and observed gravity anomalies provides an independent method for evaluating velocity models and potentially offers insights into geological structures (Lo et al., 2021; Yen & Hsieh, 2010). In this study, we conducted comparative analyses using three tomographic models: Kuo-Chen et al. (2012), Huang et al. (2014), and our current model. To facilitate this comparison, we converted the P-wave velocities from the velocity models into density models using established empirical relationships between P-wave velocity and rock density (Brocher, 2005). The analysis utilized an updated Bouguer anomaly data set for Taiwan, which incorporates more accurate terrain data for improved precision (Yen & Hsieh, 2010). For standardized comparison, P-wave velocities were linearly interpolated onto a uniform grid with 1 km spacing, and gravity anomalies were calculated for depths ranging from 0 to 60 km. Correlation analysis between the observed and calculated Bouguer anomalies yielded coefficients of approximately 0.37 for Kuo-Chen et al. (2012), 0.66 for Huang et al. (2014), and 0.74 for our tomographic model (Figures 9a–9d). These results suggest that our model demonstrates better agreement with observed gravity anomalies compared to the previous models.

In addition, gravity forward calculations may provide valuable insights into the gravity performance of velocity models and contribute to understanding geological structures in the study area (e.g., Lo et al., 2021). In this study, we performed separate forward calculations for the upper crust (0–20 km) and middle to lower crust (20–60 km) based on our velocity model to analyze gravity anomalies and their geological implications (Figures 9e and 9f). The upper crustal analysis reveals distinct gravity patterns across different geological regions. The Coastal Plain and Western Foothills regions predominantly show relatively low gravity anomalies. In contrast, the Peikang Basement High region exhibits higher gravity anomalies, consistent with its relatively shallow sedimentary cover (Figure 9e). These gravity anomalies show notable consistency with basement structure estimations proposed by Lin et al. (2003). Lower gravity anomalies are observed in the Taishi Basin to the north and the Tainan Basin to the south, reflecting their thicker sedimentary deposits (e.g., Lin et al., 2003; Yang et al., 2006). Particularly notable are the significantly low gravity values in the Pingtung Plain, corresponding to substantial sedimentary accumulation in this region. The mountainous regions display relatively high gravity anomalies, consistent with Taiwan's geological units, likely reflecting variations in rock composition.

Analysis of the middle to lower crust (20–60 km) reveals distinctive features, particularly notable relatively low gravity anomalies beneath the mountain regions from 22.5°N to 24.5°N, reflecting crustal thickening (Figure 9f). More pronounced negative gravity anomalies in the northern part suggest enhanced crustal thickening in this region. These observations align well with previous tomographic studies (e.g., Huang et al., 2014; Kim et al., 2005; Koulakov et al., 2015; Kuo-Chen et al., 2012; Rau & Wu, 1995; Roecker et al., 1987; Wu et al., 2007,

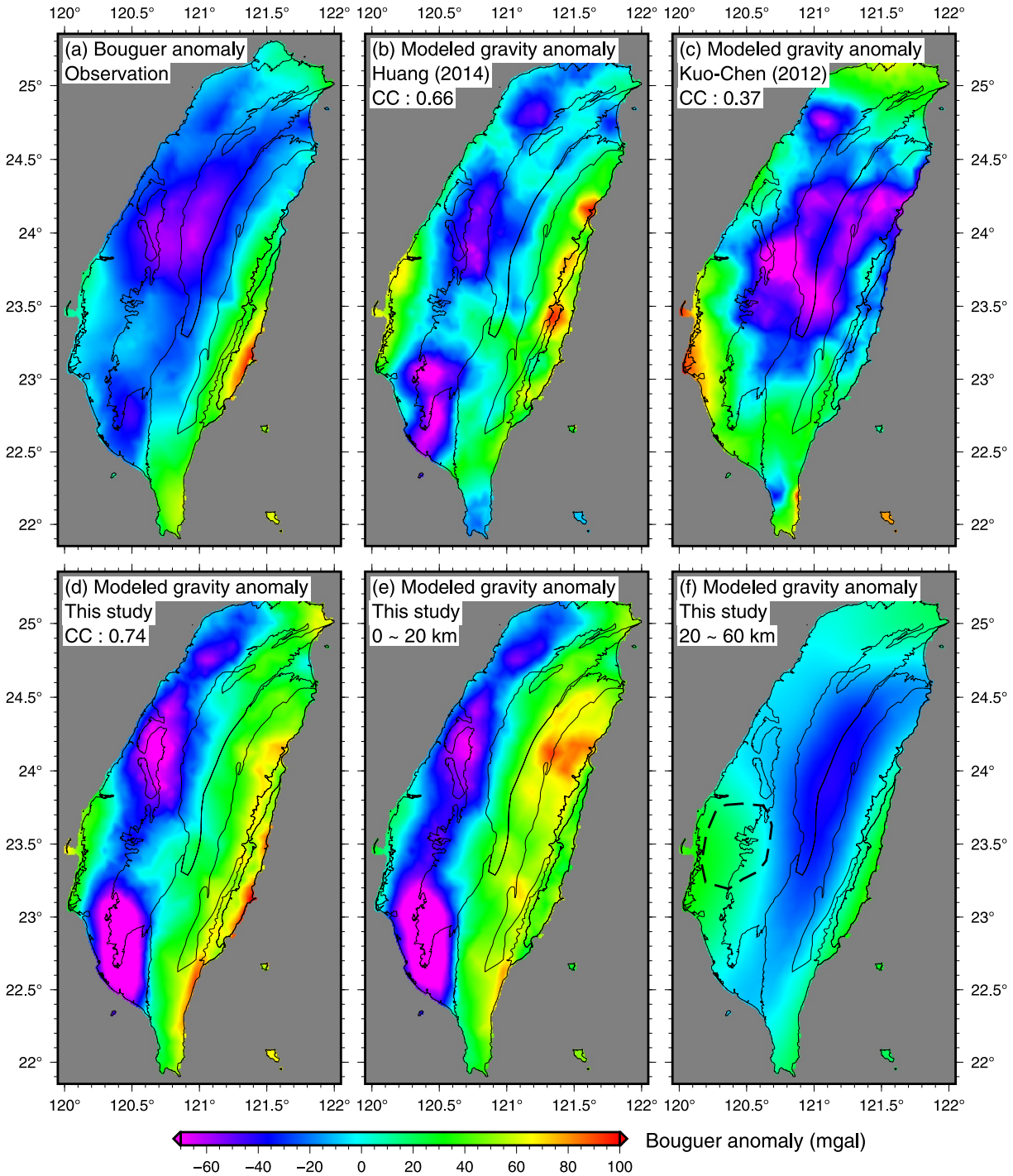

Figure 9. (a) Observed Bouguer gravity anomalies across Taiwan (Yen & Hsieh, 2010). (b)–(d) Modeled Bouguer gravity anomalies based on Vp models at depths of 0–60 km from Huang et al. (2014), Kuo-Chen et al. (2012), and this study, respectively. The CC represents the correlation coefficient between observed and modeled gravity anomalies. (e) Modeled Bouguer gravity anomalies derived from the Vp model of this study at depths of 0–20 km. (f) Modeled Bouguer gravity anomalies derived from the Vp model of this study at depths of 20–60 km. The dashed line indicates a region associated with a relatively high-velocity anomaly in our model.

2009), providing additional validation of our model's reliability. Our velocity model also reveals relatively high gravity anomalies in west-central Taiwan (Figure 9f), consistent with the possible high-density body suggested in previous gravity analyses (Hsieh & Yen, 2016). These gravity forward calculations reinforce our model's

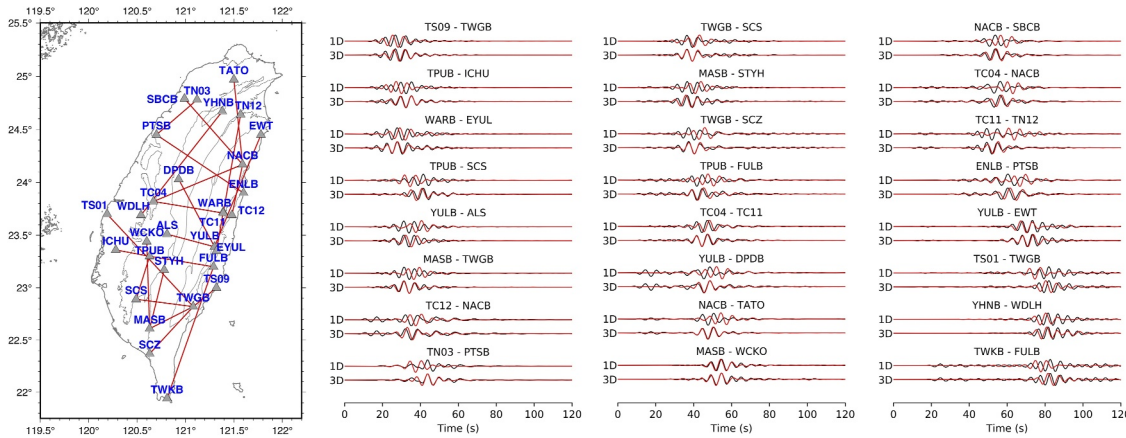

Figure 10. Waveform comparisons of synthetic and observed empirical Green's functions. The map shows the station pairs of the empirical Green's functions. The black lines represent the observed empirical Green's functions, while the red lines represent the corresponding synthetic waveforms calculated using the 1D layered model and our 3D velocity model.

consistency with known geological features, including crustal thickening patterns and sedimentary variations in plains and basins.

4.3.2. Model Evaluations Using Waveform Simulations

Advances in numerical simulation methods and computing capabilities have enabled the simulation of seismic wave propagation in complex 3D velocity models. These seismic wave simulations can also be used to evaluate the accuracy and reliability of 3D velocity models. In this study, we employ empirical Green's functions (EGFs), obtained by stacking cross-correlation functions of ambient noise (e.g., Bensen et al., 2007; Schimmel et al., 2011), for model evaluations. The EGFs are calculated among the broadband stations. A similar validation approach has been applied in evaluating velocity models of southern California (e.g., Ma et al., 2008). Since the EGFs are not used in our tomographic inversions, the results provide an independent evaluation of our velocity model.

For the waveform comparisons, we utilize the SW4 (Seismic Waves, 4th order) code (Petersson & Sjögreen, 2014) for seismic waveform simulations of EGFs, considering the topography in the simulations. The waveforms are bandpassed at corner frequencies between 0.1 and 0.2 Hz. Figure 10 presents examples of waveform comparisons among data waveforms and those generated from the initial 1D layered model and our 3D model. The waveforms of the 3D model show significant improvements compared to those of the 1D layered model, reflecting the enhancements in the velocity model at the crustal scale. The improvements in the velocity model not only provide a more reliable initial model for future full-wave-based tomographic inversions but also serve as a reference model for centroid moment tensor inversions using waveforms of the 3D model (e.g., Lee et al., 2011, 2014). These advancements in velocity modeling contribute to a better understanding of the complex seismic structure and the accuracy of seismic source parameter estimations in the study region.

5. Discussions

5.1. Inferred Crustal Structures From Tomographic Velocity Gradients

Our seismic tomographic results reproduce many crustal features reported in previous studies, supporting the reliability of the model. In addition, the velocity model benefits from dense station coverage, a large number of seismic phase picks, and a refined inversion setup, yielding improved resolution. This enables more refined structural interpretations, particularly in the upper crust where the resolving capability is relatively stronger (see Text S2 in Supporting Information S1, spike test). To constrain the potential structures, velocity gradients observed in our tomographic profiles are compared with surface fault traces and mapped geological unit boundaries (Figure 7, profiles Aa–Dd). For these interpretations, we relied primarily on Vs, which provides stronger velocity constraints in our model, while Vp shows a consistent overall trend (see Text S4 in Supporting Information S1; Figure 7). The interpreted fault or contact traces inferred from the velocity gradients are indicated

by dashed lines, while question marks denote uncertainties in their depth extent (Figure 7). Below, we present the inferred faults and structural contacts, organized from south to north across the Aa–Dd profiles (Figure 7).

Profile Aa (southern Taiwan): Three major structures can be identified from west to east. The westernmost inferred structure lies near the boundary between the Pingtung Plain (PP) and the Central Range (CR), close to the Chaochou Fault (CF). The central structure aligns spatially with the Tayulin Fault (TF) (Lee et al., 2022). The easternmost structure lies near the CR–Southern Longitudinal Trough (SLT) boundary. The slightly west-dipping feature inferred from the tomographic contours is relatively subtle (Text S4 in Supporting Information S1). Additional investigation will be required to further clarify the detailed structural geometry and its tectonic implications.

Profile Bb: Four major inferred structures are identified. From west to east: (a) the transition zone between the Coastal Plain (CP) and the Western Foothills (WF); (b) the WF–CR boundary; (c) a structure within the CR, spatially consistent with the TF; and (d) a west-dipping feature also imaged in the Vp/Vs ratio near the Longitudinal Valley (LV), likely representing the Central Range Fault (CRF). The west-dipping geometry inferred from the tomographic contours is relatively subtle (Text S4 in Supporting Information S1), and additional investigation will be necessary to further constrain its detailed structural geometry.

Profile Cc: Four structures are inferred from west to east. (a) The CP–WF boundary; (b) the WF–Hsueshan Range (HR) boundary; (c) a feature near the HR–CR boundary and the TF; and (d) a west-dipping feature also observed in the Vp/Vs ratio near the LV, likely representing the CRF.

Profile Dd: This profile is largely comparable to the Taiwan orogen modeling results of Tan et al. (2024; their Figure 3d). The inferred structures show notable consistency with Tan et al.'s (2024) modeling results. From west to east: (a) near the front of the WF; (b) a structure near the Sanyi Fault region; (c) a feature spatially aligned with the WF–HR boundary; (d) a structure near the HR–CR boundary and the TF; and (e) a west-dipping feature also imaged in the Vp/Vs ratio near the LV.

5.2. Observed Seismicity and Stress Rotation Related to a Mid-Crustal High-Velocity Block in West-Central Taiwan

The Peikang Basement High, recognized as a relatively rigid structural feature, is associated with significantly lower seismic activity compared to the surrounding regions (Figure 11a), consistent with its interpretation as a mechanically strong basement block (e.g., Biete et al., 2019; Brown et al., 2017; Yang et al., 2006). A similar pattern is observed in our tomographic model, where a mid-crustal (~20–30 km) high-velocity zone characterized by elevated Vp and Vs values is imaged beneath west-central Taiwan. Within this zone, seismicity below 20 km is markedly reduced relative to adjacent areas (Figures 11b and 11c). Chen et al. (2017) conducted stress inversions based on earthquake focal mechanisms, using a grid resolution of 0.1° horizontally and 10 km vertically. Their analysis revealed a distinct change in the orientation of the maximum compressive stress axis above and below 20 km depth near the northern boundary of the high-velocity zone imaged in our model. The close spatial association of elevated seismic velocities, increased density (Hsieh & Yen, 2016), reduced seismicity, and stress rotation (Chen et al., 2017) suggests a relationship with compositional contrasts, although the reactivation of pre-existing faults cannot be excluded. Based on our lithological analysis (Figure 8), this mid-crustal high-velocity body is plausibly composed of mafic materials, as suggested by its map-view spatial overlap with basalts intersected at shallow depth in well K1, reported by Wang et al. (2012). These depth-dependent stress variations are broadly consistent with the extent of the high-velocity zone and are likely influenced by compositional contrasts. Such compositional heterogeneity has been shown to influence regional stress fields and deformation styles in other orogenic systems (e.g., Lacombe & Bellahsen, 2016; Mouthereau & Lacombe, 2006). The mid-crustal high-velocity anomaly in west-central Taiwan may play a critical role in modulating strain accumulation and seismicity distribution, thereby influencing the processes of orogenesis in Taiwan.

5.3. Passive-Margin Inheritance of the Mid-Crustal Anomaly: Geophysical and Geochemical Evidence From Dongsha and West-Central Taiwan

Along many rifted continental margins worldwide, high-velocity lower crust (HVLC) is generally interpreted as mafic intrusions or underplated magmas emplaced during continental breakup (e.g., Brune et al., 2017; Sapin et al., 2021; White et al., 2008). Volcanic or magma-rich margins typically exhibit thick and laterally continuous

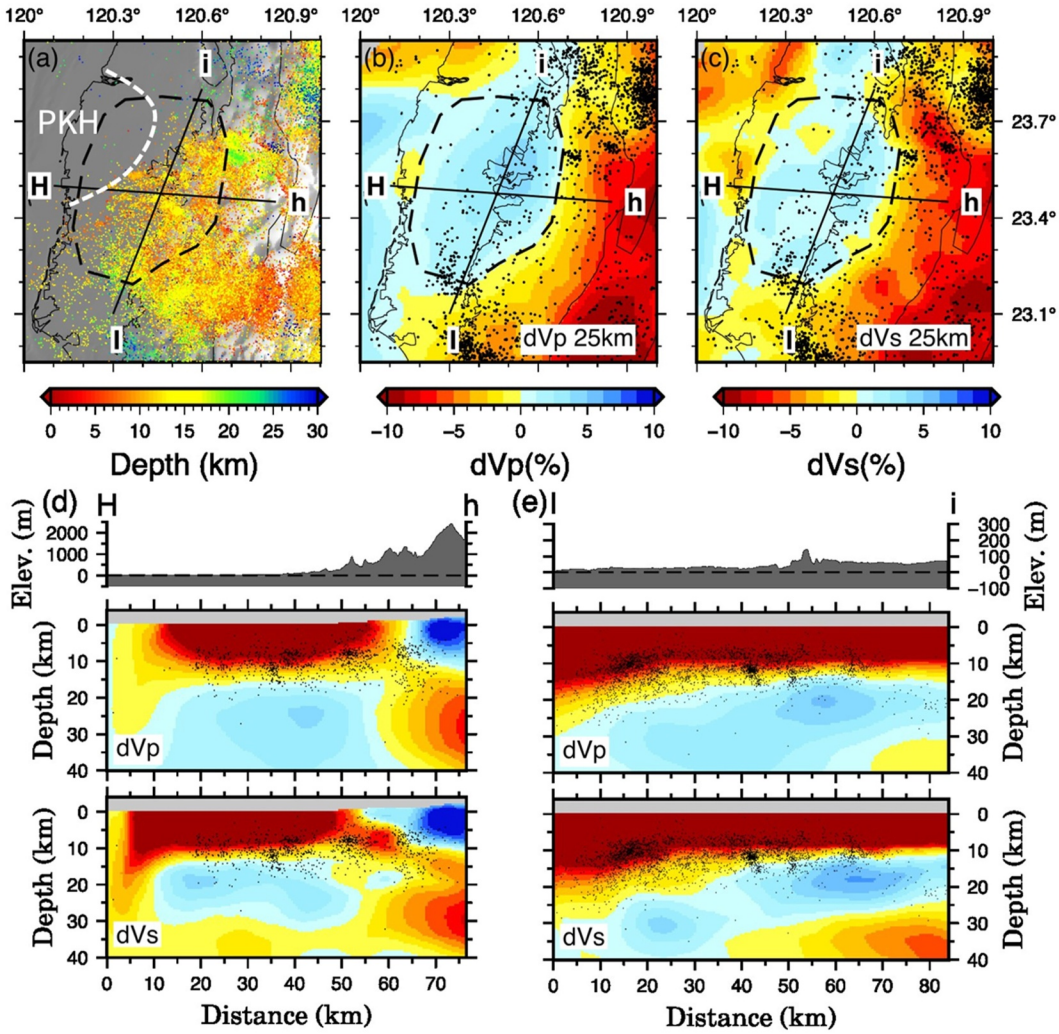

Figure 11. (a) Spatial distribution of earthquakes in west-central Taiwan (b)–(c) Horizontal maps of Vp and Vs velocity perturbations at a depth of 25 km, shown as deviations from the initial 1D layered model. Black dots indicate earthquake epicenters with focal depths exceeding 20 km. White dashed line denotes the Peikang High (PKH); black dashed lines outline the mid-crustal high-velocity anomaly. (d)–(e) Vertical profiles of Vp and Vs perturbations along selected cross-sections, presented as deviations from the initial 1D layered model. Black dots represent earthquakes located within 5 km of the respective profile planes.

HVLC beneath the continent–ocean transition (COT), whereas magma-poor margins are characterized by exhumed mantle beneath strongly thinned continental crust (Brune et al., 2017; Tugend et al., 2024). The northern margin of the South China Sea has often been regarded as an intermediate or transitional case between these two end-member types (e.g., Chang et al., 2017; Gao et al., 2015). Geophysical observations reveal pronounced HVLC beneath certain segments of the margin, while other areas display weaker or even absent HVLC expression (e.g., Chang et al., 2017; Chang et al., 2024; Gao et al., 2015). This pronounced spatial variability indicates that magmatic addition was not uniformly distributed along the margin, supporting its classification as a transitional case between classic magma-rich and magma-poor rifted margins.

West-central Taiwan and the Dongsha Rise both lie on the Eurasian passive continental margin (Figure 1) (e.g., Byrne et al., 2011; Lin et al., 2003; Lin & Watts, 2002). Along the northern South China Sea margin, multi-channel seismic and gravity studies consistently report mid-to lower-crustal high-velocity/high-density layers with variable thickness (~2 to >12 km) at ~10–30 km depth, commonly interpreted as mafic underplating (e.g., Chang et al., 2017; Fan et al., 2017; Gao et al., 2015; Xia et al., 2018). The depth range of these layers matches the high-velocity body imaged beneath west-central Taiwan in our tomographic results. Furthermore, a 3D

anisotropic model (Koulakov et al., 2015) images a coast-perpendicular (margin-normal) anisotropy beneath west-central Taiwan, spatially coincident with the Peikang Basement High in the upper crust and with our mid-crustal high-velocity body at depth. If the high-velocity body is mafic-dominated (Section 4.2), its elevated density and deep origin are consistent with mafic underplating at mid-to lower-crustal depths. This interpretation may relate to post-spreading asthenospheric upwelling and associated basaltic activity in west-central Taiwan (Wang et al., 2012). The observed anisotropy may be attributed to oriented fabrics associated with underplating and likely reflects the geometry and flow direction of mafic magma emplacement during this process (e.g., Almqvist & Mainprice, 2017; Silver, 1996). We note, however, that seismic anisotropy is inherently non-unique and may also be influenced by additional factors such as localized deformation, structural heterogeneity, or subsequent tectonic modification (e.g., Savage, 1999; Silver, 1996).

In addition to the geophysical similarities, basaltic rocks have also been documented in both the Dongsha Rise (e.g., Li et al., 2022) and the Peikang Basement High region of west-central Taiwan (e.g., Wang et al., 2012; well K1). These volcanic occurrences exhibit comparable geochemical and tectonic characteristics. The Dongsha basalts are marked by ocean island basalt (OIB)-like trace element patterns and isotopic signatures consistent with contributions from an enriched mantle source (e.g., Li et al., 2022). Similarly, late Miocene basalts recovered from well K1 in the Peikang Basement High region (Wang et al., 2012) exhibit OIB-like geochemical affinities and isotopic compositions that overlap with those of South China Sea seamount basalts (Wang et al., 2012). Together, these findings suggest that basaltic magmatism in both regions was derived principally from the asthenospheric mantle, likely involving upwelling processes (e.g., Wang et al., 2012). A portion of this magma likely erupted at the surface, whereas another portion was emplaced or underplated at the base of the crust, forming mafic layers capable of sustaining high velocities and densities at mid-crustal depths.

Both the Dongsha Rise and the Peikang Basement High are structural highs developed along the passive continental margin of the Eurasian Plate (Figure 1). They exhibit consistent similarities in geophysical signatures and magmatic records, suggesting that comparable geodynamic processes were active during their formation. Integrating these observations, a plausible interpretation is that asthenospheric upwelling facilitated the emplacement and underplating of mafic magmas at the base of the crust. This process not only contributed to margin uplift but also introduced mafic additions into the mid-to lower crust in both regions (e.g., Chang et al., 2024; Lin et al., 2003; Lüdmann & Wong, 1999).

6. Conclusions

This study presents a new 3D crustal velocity model for Taiwan, developed through the integration of diverse seismic data sets and advanced data processing techniques. The model incorporates waveform data from both permanent and temporary seismic networks, including post-2012 upgrades to the Central Weather Administration Seismic Network (CWASN) and the Taiwan Strong Motion Instrumentation Program (TSMIP). These upgraded systems provide improved timing accuracy (Chang et al., 2012) and denser spatial coverage, enhancing the quality and completeness of the data set. To further improve arrival-time precision, we applied a machine learning–based phase picker specifically trained on Taiwan seismic data, which enabled the consistent and accurate selection of P- and S-wave arrivals across a large volume of events. The reliability of the velocity model has been thoroughly validated using multiple approaches. These include synthetic resolution tests (checkerboard, restoration, and spike tests), internal validation through odd–even event inversions, comparisons with independently derived gravity data, and simulations using ambient noise Green's functions. Collectively, these assessments confirm that the model achieves high spatial resolution and exhibits structural features that are both geologically plausible and geophysically consistent. Our tomographic model is broadly consistent with previously published regional studies, particularly in delineating large-scale tectonic structures (e.g., Huang et al., 2014; Kim et al., 2005; Koulakov et al., 2015; Kuo-Chen et al., 2012; Rau & Wu, 1995; Roecker et al., 1987; Wu et al., 2007, 2009). In addition, structures inferred from velocity gradients in the tomographic profiles across the Taiwan orogen largely coincide with mapped faults and geological unit boundaries. These results highlight the enhanced resolution achieved through the updated data set and methodology, enabling improved imaging of both regional and localized crustal structures.

In addition to imaging the regional crustal architecture, our model delineates a pronounced mid-crustal (~20–30 km) high-velocity anomaly beneath west-central Taiwan. This feature is characterized by elevated Vp and Vs values and is consistent with density estimates. Rock-physics comparisons under representative P–T

conditions indicate that mafic lithologies provide the closest match, although alternative interpretations cannot be excluded. Coast-perpendicular (margin-normal) seismic anisotropy reported by Koulakov et al. (2015) supports the interpretation of inherited extensional fabrics. Furthermore, geophysical and geochemical similarities with the Dongsha Rise, including mid-to lower-crustal high-velocity layers and Miocene OIB-type basalts (e.g., Li et al., 2022; Wang et al., 2012), suggest a possible shared tectono-magmatic origin linked to mantle upwelling and mafic underplating during South China Sea rifting. Finally, the mid-crustal high-velocity body coincides with reduced seismicity below ~20 km and depth-dependent stress orientations (Chen et al., 2017), implying that pre-existing passive-margin structures can persist into an active orogen and modulate both orogenic architecture and seismic behavior in Taiwan.

By comparing synthetic waveforms generated using the 3D velocity model with observed waveforms, this study provides independent validation of the model. The empirical Green's functions, which were not utilized in the tomographic inversion, serve as an independent data set for this validation (e.g., Ma et al., 2008). The synthetic waveforms derived from the 3D model show significant improvement over those generated from the initial 1D velocity model, demonstrating the reliability of the refined velocity structure. These advancements not only validate the enhancements in velocity structures but also offer more reliable synthetic waveforms for Centroid Moment Tensor (CMT) inversion and earthquake simulations (e.g., Lee et al., 2011, 2014). Additionally, the new velocity model establishes a robust foundation for future full-waveform tomography, paving the way for further improvements.

Conflict of Interest

The authors declare no conflicts of interest relevant to this study.

Data Availability Statement

The seismic recordings used in this seismic tomographic inversion are from various networks, including the CWSN and TSMIP data sets (https://gdms.cwa.gov.tw/, last accessed 17 September 2024) from CWA (Central Weather Administration, 2012), the P-alert data set (Wu et al., 2013) (https://palert.earth.sinica.edu.tw/, last accessed 17 September 2024) and the BATS data sets from IES (Institute of Earth SciencesAcademia Sinica-Taiwan, 1996) (https://tecws1.earth.sinica.edu.tw/BATSWS/, last accessed 17 September 2024), the TAIGER seismic data sets (Okaya et al., 2006), and the seismic recordings operated by the Japan Meteorological Agency Seismic Network from the EarthScope Consortium (https://ds.iris.edu/mda/, last accessed 17 September 2024). The 3D seismic velocity model from this study is available through the Taiwan Velocity Models portal (https://tecdc.earth.sinica.edu.tw/TWtomo/index.php).

Acknowledgments

En-Jui Lee and Wu-Yu Liao are supported by the National Science and Technology Council, R.O.C., under contract 113-2116-M-006-004-MY3. The waveform simulations were performed using the computational resources provided by the NCAR-Wyoming Supercomputing Center under project WYOM0163. The authors would like to acknowledge the Science College of National Cheng Kung University (NCKU Science) and the National Science and Technology Council (NSTC), Taiwan, Republic of China, for providing a fellowship to support Wu-Yu Liao's Ph.D. study. We also deeply appreciate Dr. Kenn-Ming Yang, Dr. Jennifer Kung, Dr. Kuo-En Ching, Dr. Chi-Yue Huang, Dr. Huai-Jen Yang, and Mr. De-Cheng Yi for their valuable insights and discussions. We thank Dr. Dennis Brown for providing the rock data set used in our lithological comparisons and interpretations in this study. We used OpenAI's ChatGPT to assist with language editing during manuscript preparation.

References

Abers, G. A., & Hacker, B. R. (2016). A MATLAB toolbox and excel workbook for calculating the densities, seismic wave speeds, and major element composition of minerals and rocks at pressure and temperature. *Geochemistry, Geophysics, Geosystems*, *17*(2), 616–624. https://doi.org/10.1002/2015GC006171

Almqvist, B. S. G., & Mainprice, D. (2017). Seismic properties and anisotropy of the Continental crust: Predictions based on mineral texture and rock microstructure. *Reviews of Geophysics*, *55*(2), 367–433. https://doi.org/10.1002/2016RG000552

Alvarez-Marron, J., Brown, D., Camanni, G., Wu, Y.-M., & Kuo-Chen, H. (2014). Structural complexities in a foreland thrust belt inherited from the shelf-slope transition: Insights from the Alishan area of Taiwan. *Tectonics*, *33*(7), 1322–1339. https://doi.org/10.1002/2014TC003584

Barr, T. D., & Dahlen, F. A. (1990). Constraints on friction and stress in the Taiwan fold-and-thrust belt from heat flow and geochronology. *Geology*, *18*(2), 111. https://doi.org/10.1130/0091-7613(1990)018<0111:COFASI>2.3.CO;2

Bensen, G. D., Ritzwoller, M. H., Barmin, M. P., Levshin, A. L., Lin, F., Moschetti, M. P., et al. (2007). Processing seismic ambient noise data to obtain reliable broad-band surface wave dispersion measurements. *Geophysical Journal International*, *169*(3), 1239–1260. https://doi.org/10.1111/j.1365-246X.2007.03374.x

Biete, C., Alvarez-Marron, J., Brown, D., & Kuo-Chen, H. (2018). The structure of Southwest Taiwan: The development of a fold-and-thrust Belt on a margins outer Shelf and slope. *Tectonics*, *37*(7), 1973–1993. https://doi.org/10.1029/2017TC004910

Biete, C., Brown, D., Lund, B., Alvarez-Marron, J., Wu, Y.-M., Kuo-Chen, H., & Ho, C.-W. (2019). The influence of inherited continental margin structures on the stress and strain fields of the south-central Taiwan fold-and-thrust belt. *Geophysical Journal International*, *219*(1), 430–448. https://doi.org/10.1093/gji/ggz296

Brocher, T. M. (2005). Empirical relations between elastic wavespeeds and density in the Earth's crust. *Bulletin of the Seismological Society of America*, *95*(6), 2081–2092. https://doi.org/10.1785/0120050077

Brown, D., Alvarez-Marron, J., Biete, C., Kuo-Chen, H., Camanni, G., & Ho, C.-W. (2017). How the structural architecture of the Eurasian continental margin affects the structure, seismicity, and topography of the south central Taiwan fold-and-thrust belt. *Tectonics*, *36*(7), 1275–1294. https://doi.org/10.1002/2017TC004475

Brown, D., Alvarez-Marron, J., Camanni, G., Biete, C., Kuo-Chen, H., & Wu, Y.-M. (2022). Structure of the south-central Taiwan fold-and-thrust belt: Testing the viability of the model. *Earth-Science Reviews*, *231*, 104094. https://doi.org/10.1016/j.earscirev.2022.104094

Brown, D., Alvarez-Marron, J., Schimmel, M., Wu, Y.-M., & Camanni, G. (2012). The structure and kinematics of the central Taiwan mountain belt derived from geological and seismicity data. *Tectonics*, *31*(5), TC5013. https://doi.org/10.1029/2012TC003156

Brown, D., Camanni, G., Kuo-Chen, H., & Alvarez-Marron, J. (2024). A petrophysical study of the composition of Taiwan's middle and lower crust. *Tectonophysics*, *870*, 230160. https://doi.org/10.1016/j.tecto.2023.230160

Brown, D., & Ryan, P. D. (2011). *Arc-Continent collision*. Springer. https://doi.org/10.1007/978-3-540-88558-0

Brune, S., Heine, C., Clift, P. D., & Pérez-Gussinyé, M. (2017). Rifted margin architecture and crustal rheology: Reviewing Iberia-Newfoundland, Central South Atlantic, and South China Sea. *Marine and Petroleum Geology*, *79*, 257–281. https://doi.org/10.1016/j.marpetgeo.2016.10.018

Byrne, T., Chan, Y.-C., Rau, R.-J., Lu, C.-Y., Lee, Y.-H., & Wang, Y.-J. (2011). The arc–continent collision in Taiwan. In D. Brown & P. D. Ryan (Eds.), *Arc-Continent collision* (pp. 213–245). Springer Berlin Heidelberg. https://doi.org/10.1007/978-3-540-88558-0_8

Camanni, G., Alvarez-Marron, J., Brown, D., Ayala, C., Wu, Y.-M., & Hsieh, H.-H. (2016). The deep structure of south-central Taiwan illuminated by seismic tomography and earthquake hypocenter data. *Tectonophysics*, *679*, 235–245. https://doi.org/10.1016/j.tecto.2015.09.016

Carena, S., Suppe, J., & Kao, H. (2002). Active detachment of Taiwan illuminated by small earthquakes and its control of first-order topography. *Geology*, *30*(10), 935–938. https://doi.org/10.1130/0091-7613(2002)030<0935:adotib>2.0.co;2

Central Weather Administration (CWA, Taiwan). (2012). Central weather Administration seismographic network [Dataset]. *International Federation of Digital Seismograph Networks*. https://doi.org/10.7914/SN/T5

Chang, C.-H., Wu, Y.-M., Chen, D.-Y., Shin, T.-C., Chin, T.-L., & Chang, W.-Y. (2012). An examination of telemetry delay in the central weather Bureau Seismic network. *Terrestrial, Atmospheric and Oceanic Sciences*, *23*(3), 261. https://doi.org/10.3319/TAO.2011.11.29.01(T

Chang, J.-H., Hong, Z.-L., Mirza, A., Lin, L.-F., Hsieh, H.-H., Ko, J. Y.-T., et al. (2024). Spatial distribution and possible origin of the high velocity lower crust in the northern margin of the South China Sea. *Geoscience Letters*, *11*(1), 51. https://doi.org/10.1186/s40562-024-00364-4

Chang, J.-H., Hsieh, H.-H., Mirza, A., Chang, S.-P., Hsu, H.-H., Liu, C.-S., et al. (2017). Crustal structure north of the Taiping Island (Itu Aba Island), southern margin of the South China Sea. *Journal of Asian Earth Sciences*, *142*, 119–133. https://doi.org/10.1016/j.jseaes.2016.08.005

Chen, S. K., Wu, Y.-M., Hsu, Y.-J., & Chan, Y.-C. (2017). Current crustal deformation of the Taiwan orogen reassessed by cGPS strain-rate estimation and focal mechanism stress inversion. *Geophysical Journal International*, *210*(1), 228–239. https://doi.org/10.1093/gji/ggx165

Cheng, W.-B. (2004). Crustal structure of the high magnetic Anomaly Belt, Western Taiwan, and its implications for Continental Margin deformation. *Marine Geophysical Researches*, *25*(1–2), 79–93. https://doi.org/10.1007/s11001-005-0735-3

Cheng, W.-B., Huang, H.-C., Wang, C., Wu, M.-S., & Hsiuan, T.-H. (2003). Velocity structure, seismicity, and fault structure in the Peikang high area of Western Taiwan. *Terrestrial, Atmospheric and Oceanic Sciences*, *14*(1), 063. https://doi.org/10.3319/TAO.2003.14.1.63(T)

Doo, W.-B., Huang, Y.-S., Wu, W.-N., Cheng, C.-Y., Lo, C.-L., Wang, H.-F., et al. (2025). The significance of the high-amplitude magnetic anomaly belt in the seismotectonics of mid-west Taiwan. *Journal of Asian Earth Sciences*, *288*, 106598. https://doi.org/10.1016/j.jseaes.2025.106598

Eakin, D. H., McIntosh, K. D., Van Avendonk, H. J. A., Lavier, L., Lester, R., Liu, C.-S., & Lee, C.-S. (2014). Crustal-scale seismic profiles across the Manila subduction zone: The transition from intraoceanic subduction to incipient collision. *Journal of Geophysical Research: Solid Earth*, *119*(1), 1–17. https://doi.org/10.1002/2013JB010395

Fan, C., Xia, S., Zhao, F., Sun, J., Cao, J., Xu, H., & Wan, K. (2017). New insights into the magmatism in the northern margin of the S outh C hina S ea: Spatial features and volume of intraplate seamounts. *Geochemistry, Geophysics, Geosystems*, *18*(6), 2216–2239. https://doi.org/10.1002/2016GC006792

Gao, J., Wu, S., McIntosh, K., Mi, L., Yao, B., Chen, Z., & Jia, L. (2015). The continent–ocean transition at the mid-northern margin of the South China Sea. *Tectonophysics*, *654*, 1–19. https://doi.org/10.1016/j.tecto.2015.03.003

Ho, C. S. (1986). A synthesis of the geologic evolution of Taiwan. *Tectonophysics*, *125*(1), 1–16. https://doi.org/10.1016/0040-1951(86)90004-1

Hsieh, H.-H., & Yen, H.-Y. (2016). Three-dimensional density structures of Taiwan and tectonic implications based on the analysis of gravity data. *Journal of Asian Earth Sciences*, *124*, 247–259. https://doi.org/10.1016/j.jseaes.2016.05.009

Hsu, S.-K., Liu, C.-S., Shyu, C.-T., Liu, S.-Y., Sibuet, J.-C., Lallemand, S., et al. (1998). New gravity and magnetic Anomaly maps in the Taiwan-Luzon Region and their preliminary interpretation. *Terrestrial, Atmospheric and Oceanic Sciences*, *9*(3), 509. https://doi.org/10.3319/TAO.1998.9.3.509(TAICRUST

Hsu, S.-K., Yeh, Y.-C., Lo, C.-L., Lin, A. T.-S., & Doo, W.-B. (2008). Link between crustal magnetization and earthquakes in Taiwan. *Terrestrial, Atmospheric and Oceanic Sciences*, *19*(5), 445. https://doi.org/10.3319/TAO.2008.19.5.445(T)

Huang, C.-Y., Wu, W.-Y., Chang, C.-P., Tsao, S., Yuan, P. B., Lin, C.-W., & Xia, K.-Y. (1997). Tectonic evolution of accretionary prism in the arc-continent collision terrane of Taiwan. *Tectonophysics*, *281*(1), 31–51. https://doi.org/10.1016/s0040-1951(97)00157-1

Huang, H.-H., Wu, Y.-M., Song, X., Chang, C.-H., Lee, S.-J., Chang, T.-M., & Hsieh, H.-H. (2014). Joint Vp and Vs tomography of Taiwan: Implications for subduction-collision orogeny. *Earth and Planetary Science Letters*, *392*, 177–191. https://doi.org/10.1016/j.epsl.2014.02.026

Institute of Earth Sciences, Academia Sinica, Taiwan. (1996). Broadband array in Taiwan for seismology. *Institute of Earth Sciences, Academia Sinica, Taiwan. Other/Seismic Network*. https://doi.org/10.7914/SN/TW

Kao, H., Jian, P.-R., Ma, K.-F., Huang, B.-S., & Liu, C.-C. (1998). Moment-tensor inversion for offshore earthquakes east of Taiwan and their implications to regional collision. *Geophysical Research Letters*, *25*(19), 3619–3622. https://doi.org/10.1029/98GL02803

Kim, K.-H., Chiu, J.-M., Pujol, J., Chen, K.-C., Huang, B.-S., Yeh, Y.-H., & Shen, P. (2005). Three-dimensional V Pand V Sstructural models associated with the active subduction and collision tectonics in the Taiwan region. *Geophysical Journal International*, *162*(1), 204–220. https://doi.org/10.1111/j.1365-246X.2005.02657.x

Koulakov, I. (2009). LOTOS code for local earthquake tomographic inversion: Benchmarks for testing tomographic AlgorithmsLOTOS code for local earthquake tomographic inversion: Benchmarks for testing tomographic algorithms. *Bulletin of the Seismological Society of America*, *99*(1), 194–214. https://doi.org/10.1785/0120080013

Koulakov, I., Jakovlev, A., Wu, Y.-M., Dobretsov, N. L., El Khrepy, S., & Al-Arifi, N. (2015). Three-dimensional seismic anisotropy in the crust and uppermost mantle beneath the Taiwan area revealed by passive source tomography: 3-D anisotropic structure OF the TAIWAN. *Journal of Geophysical Research: Solid Earth*, *120*(11), 7814–7829. https://doi.org/10.1002/2015JB012408

Koulakov, I., Wu, Y.-M., Huang, H.-H., Dobretsov, N., Jakovlev, A., Zabelina, I., et al. (2014). Slab interactions in the Taiwan region based on the P- and S-velocity distributions in the upper mantle. *Journal of Asian Earth Sciences*, *79*, 53–64. https://doi.org/10.1016/j.jseaes.2013.09.026

Kuo-Chen, H., Wu, F. T., & Roecker, S. W. (2012). Three-dimensional P velocity structures of the lithosphere beneath Taiwan from the analysis of TAIGER and related seismic data sets: 3D VP structures from TAIGER project. *Journal of Geophysical Research*, *117*(B6). https://doi.org/10.1029/2011JB009108

Lacombe, O., & Bellahsen, N. (2016). Thick-skinned tectonics and basement-involved fold–thrust belts: Insights from selected Cenozoic orogens. *Geological Magazine*, *153*(5–6), 763–810. https://doi.org/10.1017/S0016756816000078

Lacombe, O., Mouthereau, F., Angelier, J., Chu, H., & Lee, J. (2003). Frontal belt curvature and oblique ramp development at an obliquely collided irregular margin: Geometry and kinematics of the NW Taiwan fold-thrust belt. *Tectonics*, *22*(3), 2002TC001436. https://doi.org/10.1029/2002TC001436

Lallemand, S., Font, Y., Bijwaard, H., & Kao, H. (2001). New insights on 3-D plates interaction near Taiwan from tomography and tectonic implications. *Tectonophysics*, *335*(3), 229–253. https://doi.org/10.1016/s0040-1951(01)00071-3

Lallemand, S., Theunissen, T., Schnürle, P., Lee, C.-S., Liu, C.-S., & Font, Y. (2013). Indentation of the Philippine Sea plate by the Eurasia plate in Taiwan: Details from recent marine seismological experiments. *Tectonophysics*, *594*, 60–79. https://doi.org/10.1016/j.tecto.2013.03.020

Lee, E.-J., Chen, P., Jordan, T. H., Maechling, P. B., Denolle, M. A. M., & Beroza, G. C. (2014). Full-3-D tomography for crustal structure in Southern California based on the scattering-integral and the adjoint-wavefield methods. *Journal of Geophysical Research: Solid Earth*, *119*(8), 6421–6451. https://doi.org/10.1002/2014JB011346

Lee, E.-J., Chen, P., Jordan, T. H., & Wang, L. (2011). Rapid full-wave centroid moment tensor (CMT) inversion in a three-dimensional earth structure model for earthquakes in Southern California. *Geophysical Journal International*, *186*(1), 311–330. https://doi.org/10.1111/j.1365-246X.2011.05031.x

Lee, E.-J., Liao, W.-Y., Chen, P., Rau, R.-J., Lee, Y.-H., Wen, S., et al. (2025). Fast report: Applying a weighted template-matching algorithm (WTMA) to investigate the seismogenic structures and microseismic activity of the 2025 ML6.4 Dapu earthquake sequence in Taiwan. *Terrestrial, Atmospheric and Oceanic Sciences*, *36*(1), 9. https://doi.org/10.1007/s44195-025-00095-9

Lee, Y.-H., Byrne, T. B., Lo, W., Wang, S.-J., Tsao, S.-J., Chen, C.-H., et al. (2022). Out of sequence faulting in the backbone range, Taiwan: Implications for thickening and exhumation processes. *Earth and Planetary Science Letters*, *594*, 117711. https://doi.org/10.1016/j.epsl.2022.117711

Li, G., Mei, L., Pang, X., Zheng, J., Ye, Q., & Hao, S. (2022). Magmatism within the northern margin of the South China Sea during the post-rift stage: An overview, and new insights into the geodynamics. *Earth-Science Reviews*, *225*, 103917. https://doi.org/10.1016/j.earscirev.2022.103917

Liao, W.-Y., Lee, E.-J., Chen, D.-Y., Chen, P., Mu, D., & Wu, Y.-M. (2022). RED-PAN: Real-time earthquake detection and phase-picking with multitask attention network. *IEEE Transactions on Geoscience and Remote Sensing*, *60*, 1–11. https://doi.org/10.1109/TGRS.2022.3205558

Liao, W.-Y., Lee, E.-J., Mu, D., Chen, P., & Rau, R.-J. (2021). ARRU phase picker: Attention recurrent-residual U-Net for picking seismic *P* - And *S* -Phase arrivals. *Seismological Research Letters*, *92*(4), 2410–2428. https://doi.org/10.1785/0220200382

Liao, W.-Y., Lee, E.-J., Rau, R.-J., Chen, D.-Y., Wen, S., Ching, K.-E., & Liang, W.-T. (2025). Fast report: Seismogenic structure of the 2025 M6.4 dapu earthquake sequence in western Taiwan revealed by a deep-learning-empowered earthquake catalog. *Terrestrial, Atmospheric and Oceanic Sciences*, *36*(1), 10. https://doi.org/10.1007/s44195-025-00093-x

Lin, A. T., & Watts, A. B. (2002). Origin of the West Taiwan basin by orogenic loading and flexure of a rifted continental margin: Taiwan foreland flexure. *Journal of Geophysical Research*, *107*(B9), ETG2-1–ETG2-19. https://doi.org/10.1029/2001JB000669

Lin, A. T., Watts, A. B., & Hesselbo, S. P. (2003). Cenozoic stratigraphy and subsidence history of the South China Sea margin in the Taiwan region: Cenozoic stratigraphy of Taiwan. *Basin Research*, *15*(4), 453–478. https://doi.org/10.1046/j.1365-2117.2003.00215.x

Liu, K.-S., Shin, T.-C., & Tsai, Y.-B. (1999). A free-field strong motion network in Taiwan: Tsmip. *Terrestrial, Atmospheric and Oceanic Sciences*, *10*(2), 377–396. https://doi.org/10.3319/tao.1999.10.2.377(t)

Lo, Y.-T., Huang, H.-H., & Yen, H.-Y. (2021). Probing depth origin of gravity anomalies in Taiwan through 3-D coherent velocity model. *Terrestrial, Atmospheric and Oceanic Sciences*, *32*(3), 305–317. https://doi.org/10.3319/TAO.2021.04.30.01

Lüdmann, T., & Wong, H. K. (1999). Neotectonic regime on the passive continental margin of the northern South China Sea. *Tectonophysics*, *311*(1), 113–138. https://doi.org/10.1016/S0040-1951(99)00155-9

Ma, S., Prieto, G. A., & Beroza, G. C. (2008). Testing community velocity models for Southern California using the ambient seismic field. *Bulletin of the Seismological Society of America*, *98*(6), 2694–2714. https://doi.org/10.1785/0120080947

Malavieille, J., Lallemand, S. E., Dominguez, S., Deschamps, A., Lu, C.-Y., Liu, C.-S., et al. (2002). Arc-continent collision in Taiwan: New marine observations and tectonic evolution. In T. B. Byrne & C.-S. Liu (Eds.), *Geology and geophysics of an arc-continent collision*. Geological Society of America. https://doi.org/10.1130/0-8137-2358-2.187

Mirakian, D. C., Crespi, J. M., Byrne, T. B., Huang, C., Ouimet, W. B., & Lewis, J. C. (2013). Tectonic implications of nonparallel topographic and structural curvature in the higher elevations of an active collision zone, Taiwan. *Lithosphere*, *5*(1), 49–66. https://doi.org/10.1130/L232.1

Mouthereau, F., Deffontaines, B., Lacombe, O., & Angelier, J. (2002). Variations along the strike of the Taiwan thrust belt: Basement control on structural style, wedge geometry, and kinematics. In T. B. Byrne & C.-S. Liu (Eds.), *Geology and geophysics of an arc-continent collision*. Geological Society of America. https://doi.org/10.1130/0-8137-2358-2.31

Mouthereau, F., & Lacombe, O. (2006). Inversion of the Paleogene Chinese continental margin and thick-skinned deformation in the Western Foreland of Taiwan. *Journal of Structural Geology*, *28*(11), 1977–1993. https://doi.org/10.1016/j.jsg.2006.08.007

Mouthereau, F., & Petit, C. (2003). Rheology and strength of the Eurasian continental lithosphere in the foreland of the Taiwan collision belt: Constraints from seismicity, flexure, and structural styles. *Journal of Geophysical Research*, *108*(B11), 2512. https://doi.org/10.1029/2002JB002098

Nolet, G. (1985). Solving or resolving inadequate and noisy tomographic systems. *Journal of Computational Physics*, *61*(3), 463–482. https://doi.org/10.1016/0021-9991(85)90075-0

Okaya, D., Wu, F. T., & Avendonk, H. V. (2006). Taiwan supplement #2 to TAIGER project. *International Federation of Digital Seismograph Networks*. https://doi.org/10.7914/SN/1F_2008

Paige, C. C., & Saunders, M. A. (1982). LSQR: An Algorithm for sparse Linear equations and sparse least squares. *ACM Transactions on Mathematical Software*, *8*(1), 43–71. https://doi.org/10.1145/355984.355989

Petersson, N. A., & Sjögreen, B. (2014). Super-Grid modeling of the elastic wave equation in semi-bounded domains. *Communications in Computational Physics*, *16*(4), 913–955. https://doi.org/10.4208/cicp.290113.220514a

Rau, R.-J., & Wu, F. T. (1995). Tomographic imaging of lithospheric structures under Taiwan. *Earth and Planetary Science Letters*, *133*(3), 517–532. https://doi.org/10.1016/0012-821x(95)00076-o

Roecker, S. W., Yeh, Y. H., & Tsai, Y. B. (1987). Three-dimensional P and S wave velocity structures beneath Taiwan: Deep structure beneath an arc-continent collision. *Journal of Geophysical Research*, *92*(B10), 10547–10570. https://doi.org/10.1029/JB092iB10p10547

Sapin, F., Ringenbach, J.-C., & Clerc, C. (2021). Rifted margins classification and forcing parameters. *Scientific Reports*, *11*(1), 8199. https://doi.org/10.1038/s41598-021-87648-3

Savage, M. K. (1999). Seismic anisotropy and mantle deformation: What have we learned from shear wave splitting? *Reviews of Geophysics*, *37*(1), 65–106. https://doi.org/10.1029/98rg02075

Schimmel, M., Stutzmann, E., & Gallart, J. (2011). Using instantaneous phase coherence for signal extraction from ambient noise data at a local to a global scale: Ambient noise signal extraction. *Geophysical Journal International*, *184*(1), 494–506. https://doi.org/10.1111/j.1365-246X.2010.04861.x

Shin, T.-C., Chang, C.-H., Pu, H.-C., Lin, H.-W., & Leu, P.-L. (2013). The geophysical database management system in Taiwan. *Terrestrial, Atmospheric and Oceanic Sciences*, *24*(1), 11. https://doi.org/10.3319/TAO.2012.09.20.01(T)

Silver, P. G. (1996). Seismic anisotropy beneath the continents: Probing the depths of geology. *Annual Review of Earth and Planetary Sciences*, *24*(1), 385–432. https://doi.org/10.1146/annurev.earth.24.1.385

Suppe, J. (1980). A retrodeformable cross section of northern Taiwan. *Proceedings of the Geological Society of China*, *23*, 46–55.

Suppe, J. (1981). Mechanics of Mountain building and metamorphism in Taiwan. *Memoir, Geological Society*, *4*, 67–89.

Tan, E., Lee, Y.-H., Chang, J.-B., Zheng, M.-J., & Shyu, C. J. (2024). Mountain building process of the Taiwan orogeny. *Science Advances*, *10*(35), eadp8056. https://doi.org/10.1126/sciadv.adp8056

Teng, L. S. (1990). Geotectonic evolution of late Cenozoic arc-continent collision in Taiwan. *Tectonophysics*, *183*(1), 57–76. https://doi.org/10.1016/0040-1951(90)90188-e

Tugend, J., Mohn, G., Duretz, T., Petri, B., & Le Pourhiet, L. (2024). Extension of Continental lithosphere in rifted margins: A review of thinning mechanisms. *Comptes Rendus Geoscience*, *356*(S2), 331–365. https://doi.org/10.5802/crgeos.257

Van Avendonk, H. J. A., McIntosh, K. D., Kuo-Chen, H., Lavier, L. L., Okaya, D. A., Wu, F. T., et al. (2016). A lithospheric profile across northern Taiwan: From arc-continent collision to extension. *Geophysical Journal International*, *204*(1), 331–346. https://doi.org/10.1093/gji/ggv468

Wang, K.-L., Chung, S.-L., Lo, Y.-M., Lo, C.-H., Yang, H.-J., Shinjo, R., et al. (2012). Age and geochemical characteristics of Paleogene basalts drilled from western Taiwan: Records of initial rifting at the southeastern Eurasian continental margin. *Lithos*, *155*, 426–441. https://doi.org/10.1016/j.lithos.2012.10.002

White, R. S., Smith, L. K., Roberts, A. W., Christie, P. a. F., & Kusznir, N. J. (2008). Lower-crustal intrusion on the North Atlantic continental margin. *Nature*, *452*(7186), 460–464. https://doi.org/10.1038/nature06687

Wu, F. T., Rau, R.-J., & Salzberg, D. (1997). Taiwan orogeny: Thin-skinned or lithospheric collision? *Tectonophysics*, *274*(1), 191–220. https://doi.org/10.1016/s0040-1951(96)00304-6

Wu, Y.-M., Chang, C.-H., Zhao, L., Shyu, J. B. H., Chen, Y.-G., Sieh, K., & Avouac, J.-P. (2007). Seismic tomography of Taiwan: Improved constraints from a dense network of strong motion stations. *Journal of Geophysical Research*, *112*(B8), B08312. https://doi.org/10.1029/2007JB004983

Wu, Y.-M., Chen, D.-Y., Lin, T.-L., Hsieh, C.-Y., Chin, T.-L., Chang, W.-Y., et al. (2013). A high-density seismic network for earthquake early warning in Taiwan based on low cost sensors. *Seismological Research Letters*, *84*(6), 1048–1054. https://doi.org/10.1785/0220130085

Wu, Y.-M., Shyu, J. B. H., Chang, C.-H., Zhao, L., Nakamura, M., & Hsu, S.-K. (2009). Improved seismic tomography offshore northeastern Taiwan: Implications for subduction and collision processes between Taiwan and the southernmost Ryukyu. *Geophysical Journal International*, *178*(2), 1042–1054. https://doi.org/10.1111/j.1365-246X.2009.04180.x

Xia, S., Zhao, F., Zhao, D., Fan, C., Wu, S., Mi, L., et al. (2018). Crustal plumbing system of post-rift magmatism in the northern margin of South China Sea: New insights from integrated seismology. *Tectonophysics*, *744*, 227–238. https://doi.org/10.1016/j.tecto.2018.07.002

Yang, K.-M., Huang, S.-T., Wu, J.-C., Ting, H.-H., & Mei, W.-W. (2006). Review and new insights on Foreland tectonics in Western Taiwan. *International Geology Review*, *48*(10), 910–941. https://doi.org/10.2747/0020-6814.48.10.910

Yang, K.-M., Rau, R.-J., Chang, H.-Y., Hsieh, C.-Y., Ting, H.-H., Huang, S.-T., et al. (2016). The role of basement-involved normal faults in the recent tectonics of western Taiwan. *Geological Magazine*, *153*(5–6), 1166–1191. https://doi.org/10.1017/S0016756816000637

Yen, H.-Y., & Hsieh, H.-H. (2010). A Study on the compatibility of 3-D seismic velocity structures with gravity data of Taiwan. *Terrestrial, Atmospheric and Oceanic Sciences*, *21*(6), 897. https://doi.org/10.3319/TAO.2010.03.03.01(T

Yen, H.-Y., Yeh, Y.-H., & Wu, F. T. (1998). Two-dimensional crustal structures of Taiwan from gravity data. *Tectonics*, *17*(1), 104–111. https://doi.org/10.1029/97TC02697

References From the Supporting Information

Liu, C.-N., Lin, F.-C., Huang, H.-H., Wang, Y., Berg, E. M., & Lin, C.-H. (2021). High-Resolution 3-D shear wave velocity model of Northern Taiwan via bayesian joint inversion of rayleigh wave ellipticity and phase velocity with Formosa array. *Journal of Geophysical Research: Solid Earth*, *126*(5), e2020JB021610. https://doi.org/10.1029/2020JB021610